



A possible planet candidate in an external galaxy detected through X-ray transit

Rosanne Di Stefano¹✉, Julia Berndtsson², Ryan Urquhart³, Roberto Soria^{4,5}, Vinay L. Kashyap¹⁶, Theron W. Carmichael¹⁷ and Nia Imara⁸

Many lines of reasoning suggest that external galaxies should host planetary systems, but detecting them by methods typically used in our own Galaxy is not possible. An alternative approach is to study the temporal behaviour of X-rays emitted by bright extragalactic X-ray sources, where an orbiting planet would temporarily block the X-rays and cause a brief eclipse. We report on such a potential event in the X-ray binary M51-ULS-1 in the galaxy M51. We examined a range of explanations for the observed X-ray dip, including a variety of transiting objects and enhancements in the density of gas and dust. The latter are ruled out by the absence of changes in X-ray colours, save any with sharp density gradients that cannot be probed with our data. Instead, the data are well fit by a planet transit model in which the eclipsor is most likely to be the size of Saturn. We also find that the locations of possible orbits are consistent with the survival of a planet bound to a mass-transfer binary.

Planets are ubiquitous in the Milky Way. The conditions under which the known planets formed exist in other galaxies as well. Yet each external galaxy occupies such a small area of the sky that the high projected stellar density makes it difficult to study individual stars in enough detail to detect the signatures of planets through either radial velocity measurements or transit detection, the two methods primarily responsible for the discovery of roughly 4,800 exoplanets (<http://www.exoplanet.eu>).

X-ray binaries (XRBs) may be ideal places to search for planets, because the cross-sectional areas of the X-ray-emitting regions can be comparable to or even smaller than planetary cross-sections, as suggested in ref.¹. A planet passing in front of the X-ray-emitting region may produce a total or near-total eclipse of the X-rays.

Are planets expected to inhabit XRBs? The first planets to be discovered orbit fast-spinning, millisecond radio pulsars that were once XRBs². Although the genesis of planets around neutron stars is not yet well understood, at least one of the four millisecond radio pulsars known to host planets^{3,4} is thought to have had a circumbinary planet in orbit during its X-ray binary phase⁵. This suggests that searches for planets orbiting XRBs have the potential to make discoveries. We report on a search for X-ray transits of the bright X-ray sources (XRSs) in three external galaxies, M51, M101 and M104.

The X-ray binary M51-ULS-1

M51-ULS-1 is one of the brightest XRSs in M51. Because of its brightness and almost purely thermal soft X-ray spectrum, it is classified as an ultraluminous supersoft source (ULS)^{6,7}. The source lies close to the heart of M51, one of three external galaxies (the others being M101 and M104), in which we studied the light curves of XRBs to search for transits. The X-ray observations we employed from both Chandra and XMM-Newton are summarized in Extended Data Figs. 1 and 2, which are in tabular form.

During a 190ks Chandra pointing (ObsID 13814, 2012 September 20), the X-ray light curve exhibited a fall from baseline to zero flux and then an approximately symmetric rise back to baseline. The event, shown in Fig. 1, lasted for 10–12ks. In Methods we describe our automated method to identify possible transits, and Extended Data Fig. 3 shows the light curve containing the event in context with light curves that were not selected.

The average effective radius of the X-ray-emitting region during this observation, before and after the flux dip, had been estimated to be $R_X = 2.5_{-1.1}^{+4.1} \times 10^9$ cm (90% uncertainty interval)⁷. The radius, checked again for this paper, is extracted from a fit to the broadband X-ray data collected just prior to and after the dip to zero flux.

Terashima et al.⁸ identified a counterpart to M51-ULS-1 in a Hubble Space Telescope (HST) image, consistent with stellar type B2–8. Comparison with the relevant isochrones yields an age range estimate of 4 Myr to 16 Myr. There is a high likelihood that this luminous blue object is in fact the counterpart to the XRS. First, bright soft X-ray emitters generally have counterparts that are optically bright, and a blue supergiant is one of the predicted counterparts to ultraluminous X-ray sources (ULXs)⁹. Second, based on the visual field, there is a probability of only 0.17 that a star this bright would happen to be at the location of M51-ULS-1 by chance.

In addition, the HST image of the region around M51-ULS-1, shown next to the Chandra image in Fig. 2, reveals that the source lies on the edge of a young stellar cluster surrounded by diffuse H α emission.

Nature of the X-ray dip

X-ray light curves exhibit variability of many types. Flares and long-lasting high and/or low states are observed, as are short-lasting dips that are not transits. To determine whether the characteristics of the event we identified set it apart, we compare it with other types of dipping events.

¹Institute for Theory and Computation, Center for Astrophysics | Harvard & Smithsonian, Cambridge, MA, USA. ²Department of Physics, Princeton University, Princeton, NJ, USA. ³Center for Data Intensive and Time Domain Astronomy, Department of Physics and Astronomy, Michigan State University, East Lansing, MI, USA. ⁴College of Astronomy and Space Sciences, University of the Chinese Academy of Sciences, Beijing, China. ⁵Sydney Institute for Astronomy, School of Physics, University of Sydney, Sydney, New South Wales, Australia. ⁶High Energy Astrophysics Division, Center for Astrophysics | Harvard & Smithsonian, Cambridge, MA, USA. ⁷Harvard College Observatory, Harvard University, Cambridge, MA, USA. ⁸Astronomy and Astrophysics Department, University of California Santa Cruz, Santa Cruz, CA, USA. ✉e-mail: rdistefano@cfa.harvard.edu

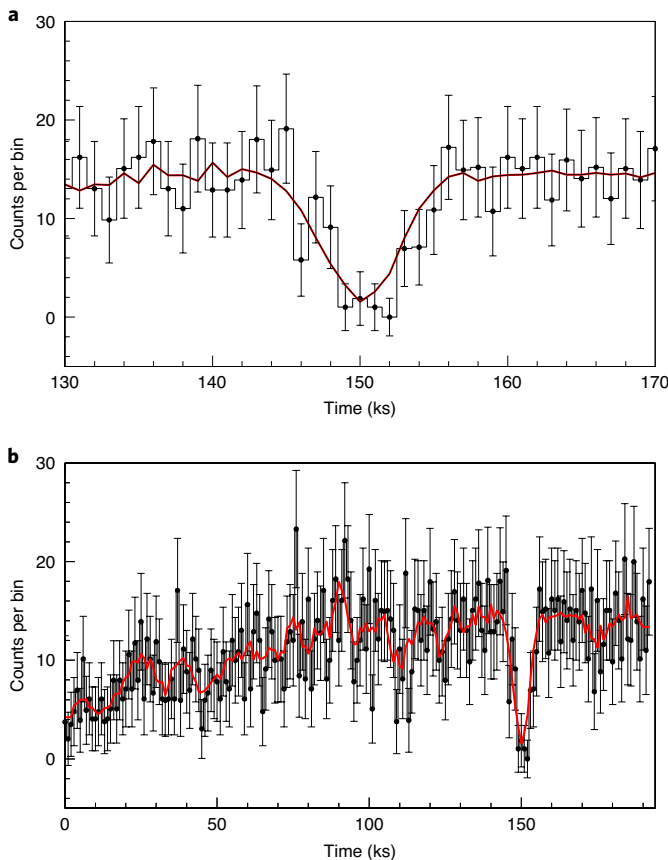


Fig. 1 | Background-subtracted X-ray light curves defined by data points for Chandra ObsID 13814. Counts in 1ks bins and the associated 1σ uncertainties are in black. The running average computed over a timescale of ± 2 ks is in red. **a**, The short-duration eclipse and roughly 20 ks on each side. **b**, The entire duration of the observation.

Accretion-related dips. The existence of irregular formations of gas and dust within XRBs has been recognized and studied for about 35 years¹⁰. Density enhancements in gas and dust (such as blobs) do not have hard surfaces or thin atmospheres, and therefore produce changes in the X-ray colour. That is, they alter the ratios between the numbers of low-energy (soft) and high-energy (hard) X-ray photons. Accretion-related dips were first observed in low-mass XRBs, binaries in which a black hole or neutron star accretes matter from a companion with mass between a few tenths of a solar mass and a few solar masses. The rate of mass transfer and the associated X-ray luminosity, L_X , tend to be lower than in ULXs, with L_X lying in the range of $10^{35}–10^{37}$ erg s $^{-1}$. Some low-mass XRBs exhibit both eclipses and dips, with single or multiple dips in flux occurring between eclipses, often within a specific range of orbital phases. Dips can differ in shape from the eclipses, and in fact exhibit a wide range of shapes¹¹, even in the light curve of a single source. The most obvious difference between a dip and an eclipse is, however, that dips display energy dependence. The spectral changes provide information about the source and the material in its close environment^{12,13}.

Accretion dips occur in other types of XRBs and even in young stars. Figure 3 shows a dipping ultraluminous soft XRS in M101, M101-ULS, exhibiting considerable intensity and spectral variability during a Chandra observation (ObsID 934). The top panel shows broadband count rate, and depicts as much as fivefold variations from maximum to minimum. The middle panel shows the spectral variations explicitly, with each dot representing a photon of a given

energy that arrived at a given time. The running median energy over the ± 16 nearest photons in time is shown as the teal curve, with vertical dotted lines marking every 17th photon. A pair of consecutive segments defined by these vertical lines form a statistically independent measurement with no correlations with a succeeding pair of segments. The bottom panel shows the fractional hardness ratio $HR = \frac{H-S}{H+S}$ covering the soft ($S=0.3–0.7$ keV) and hard ($H=0.7–3$ keV) passbands, computed as a running estimate over the nearest ± 16 (teal) and ± 32 (red) photons. Error bars are computed (blue shaded region) at each time using the Bayesian method of ref. ¹⁴. Estimates of HR and its errors are statistically independent over segment pairs with no overlap, and thus it is possible to deduce that the HR at count rate maximum and count rate minimum are statistically distinct.

The spectrum softens significantly during the dip compared to its state just prior to it. At 40 ks, the HR is ~ 0.9 . At < 30 ks, during a statistically independent interval, HR falls within the range of ± 0.5 . Additional examples of accretion-related dips are shown in Extended Data Fig. 4.

The variety of shapes and signals of energy dependence possible for accretion-related dips stand in contrast to the properties of the event in Fig. 1, whose lack of detectable spectral evolution is demonstrated in Fig. 4 and in Extended Data Fig. 5. We note, however, that the characteristics of clouds are so broad that the set of possibilities can never be completely explored and ruled out.

Intrinsic variability. In addition to variations caused by the passage of matter in front of the XRS, XRBs exhibit a wide range of intrinsic variability. Intrinsic variations generally show both intensity and spectral changes. One particular type of state common to soft XRBs is an X-ray ‘off’ state¹⁵. During observations, M51-ULS-1 exhibited at least one clear X-ray off state (830191401) for which the transition was not observed. We cannot determine whether that off state corresponded to an interval of large photosphere or to the middle portion of an eclipse. If the system was in eclipse, the eclipse lasted longer than 98 ks. There are several additional candidates for X-ray off states during observations, which included no interval of higher count rate. We make no assumptions about the nature(s) of the X-ray off states.

We consider whether the event of Fig. 1 can be explained as a manifestation of intrinsic variability. The luminosity of M51-ULS-1 declines by a factor somewhat larger than 10, whereas the thermal spectrum does not change significantly, indicating that the effective temperature is roughly constant. Thus, the physical change would be a shrinkage by a factor of roughly 3 in effective radius, and a symmetric expansion, taking place over roughly 3 h. This would be a dramatic pulsation of a source that otherwise shows no evidence of pulsations. A short-duration high-low-high transition of this type in a ULS would be a challenge for theory and has not to our knowledge been previously observed.

Transit. The short-duration event shown in Fig. 1 has several characteristics that distinguish it from common X-ray dips. To begin with, it has a well-defined baseline wherein the intensity drops and recovers to the same level as before the event. The intensity also drops to a level indistinguishable from background, unlike most accretion-related dips for which a residual emission continues to be present. Finally, as demonstrated in Fig. 4, the spectrum remains steady going into and coming out of the event, which is uncharacteristic of accretion-related dips. In particular, note that the HR values are computed as running estimates over ± 16 and ± 32 photons nearest in time. This allows us to detect possible changes in the spectrum during the drop as well as the rise back to baseline intensity in the count rate. We detect no discernible change in the HR over the duration of the event. Over the interval corresponding to the drop in intensity (145 ks to 150 ks),

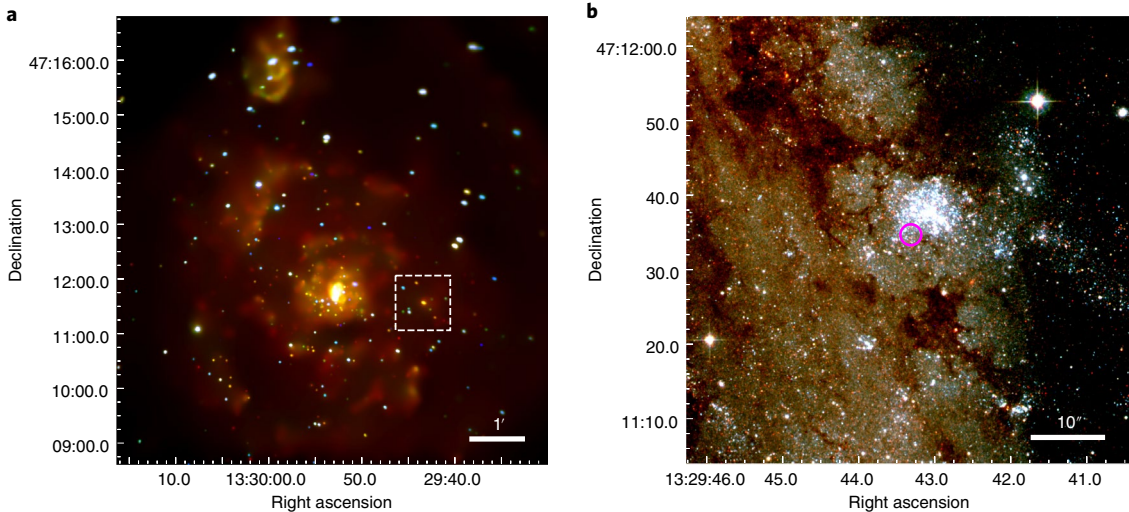


Fig. 2 | Chandra and HST images showing the region containing M51-ULS-1. **a**, False colour stacked Chandra/ACIS-S image of the Whirlpool Galaxy, M51 (total exposure of ~850 ks). Coloured points are XRSs: red is 0.3–1 keV, green is 1–2 keV and blue is 2–7 keV. M51-ULS-1 is the orange source at the centre of the $60'' \times 60''$ dashed white box. Diffuse emission is from hot gas. **b**, HST image of the area defined by the white box in **a**. Red is the F814W band, green is F555W and blue is F435W. The magenta circle marks the X-ray position of M51-ULS-1, which lies at the edge of a young star cluster. The source is located at right ascension 13:29:43.30 and declination +47:11:34.7.

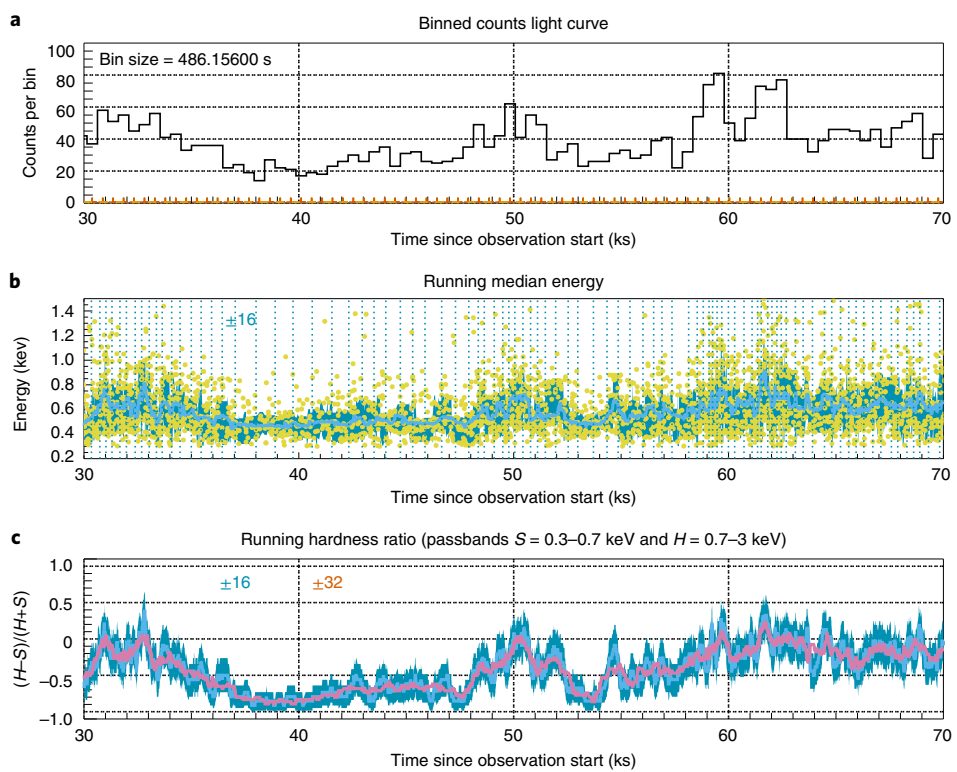


Fig. 3 | Spectral variations during an accretion dip in M101-ULS. **a**, Binned counts light curve of the source (black histogram) and estimated background (orange '+' marks), for reference. The bin size corresponds to 150 times the CCD frame readout time, and the count rate is seen to vary by a factor >4 . Grid lines are shown as dotted horizontal and vertical lines for convenience. **b**, Variation of median energy during the observation. The running median over the ± 16 nearest events (thin sky-blue curve) and the running 68% width of the spectrum (dark greenish-blue shaded area) are shown. Individual photons (greenish-yellow dots) are also shown. Every 17th event in the data stream is marked with a vertical dotted line to help delineate statistically uncorrelated periods (statistical comparisons may be carried out between paired segments of non-overlapping intervals). **c**, Hardness ratio light curve of the source, covering the passbands $S = 0.3\text{--}0.7\text{ keV}$ and $H = 0.7\text{--}3\text{ keV}$, computed using the Bayesian method of ref. ¹⁴. The 90% uncertainty band (dark-blue shaded region) computed for a running sample of ± 16 nearest neighbour photons is shown along with the estimated mean over the same window (light sky-blue curve). For comparison, a running estimate for a window of size ± 32 photons is also shown superposed (smoother magenta curve), to gauge the effect of counts fluctuations. Significant softening and hardening of the spectrum is seen in HR as the count rate dips and recovers. These variations are easily detected even using samples of 33 photons. Grid lines are shown as dotted lines for ease of comparison.

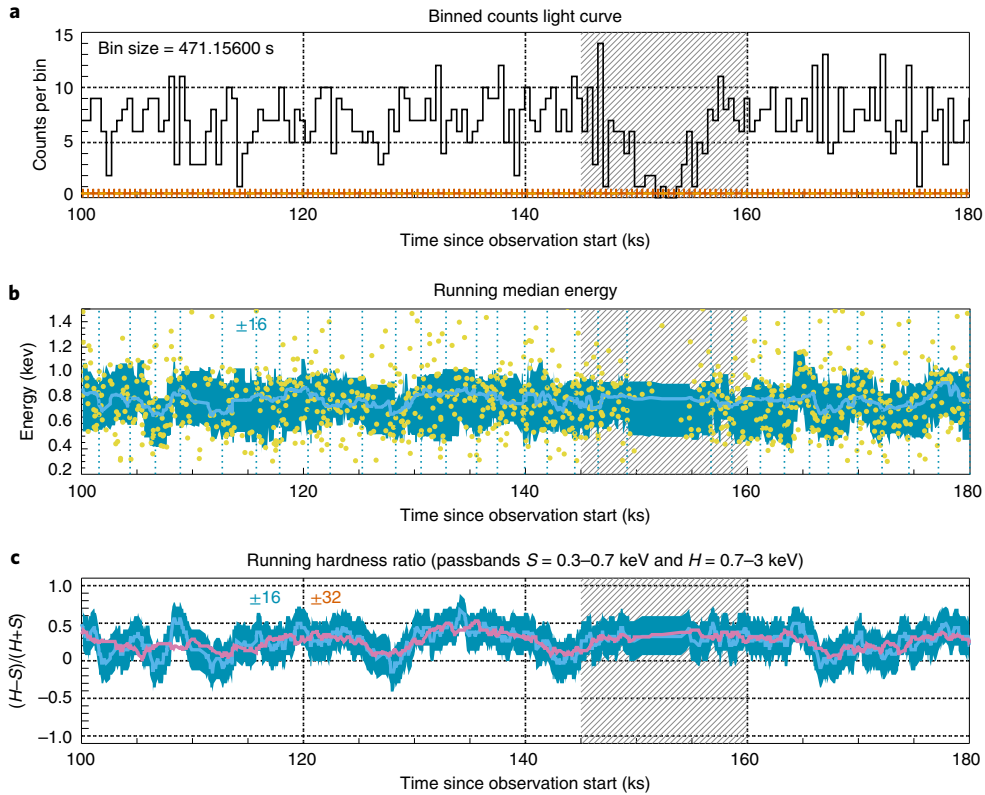


Fig. 4 | Spectral variations, or lack thereof, during the putative eclipse of the ultrasoft source M51-ULS-1. a–c, As in Fig. 3, binned counts light curve (a), running median of the photon energy (b) and hardness ratio light curve (c). The portion of the light curve dominated by the eclipse event (including both the ingress and the egress) is marked with grey hashes in all panels. Over the time interval shown, the baseline emission is steady and large intensity variations are not discernible. The variations in HR during the event are consistent with the variations seen outside the event.

the instantaneous HR fluctuates from 0.15 ± 0.27 to 0.44 ± 0.25 ; similarly over the return of the intensity to the baseline value (155 ks to 160 ks), it fluctuates between 0.2 ± 0.27 and 0.5 ± 0.24 , well within the variational range exhibited by the source prior to and after the event.

There is no evidence for a sharp change in the spectrum with intensity. Furthermore, a formal two-sample Kolmogorov–Smirnov test on the energy distributions of the photons obtained during periods of the intensity decrease, the minimum and the intensity increase, compared with the energy distributions obtained during the baseline, yields p values of 0.76, 0.93 and 0.85 respectively, showing that the spectrum obtained during the event cannot be distinguished from that outside the event. Extended Data Fig. 5 also illustrates the stability of the X-ray colours when a somewhat different approach is used.

We thus conclude that the event is characterized by a grey intensity variation unlike accretion-related dips, and that the cause of this dip is not associated with the source of the emission. These characteristics suggest that the event is caused by the passage of an opaque body with sharp borders in front of the source. Note that this type of spectral stability is also exhibited by eclipses of an XRS by its donor star. M51-ULS-1 data include evidence of both an ingress to and an egress from eclipse (Extended Data Fig. 6). Extended Data Fig. 7 demonstrates that low-level residual emission detected by XMM-Newton during the apparent eclipse may be associated with nearby XRSs, which can be resolved by Chandra but not by XMM-Newton.

A gravitationally bound solid object (a planet, brown dwarf or star) that passes in front of the XRS is expected to have a circular profile. In addition, the XRS in M51-ULS-1, whose spectrum is fit

by a thermal model, can also be well modelled in two dimensions as a circle. Deviations due to oblateness, for example, are second-order effects that cannot be reliably detected and modelled without collecting significantly more photons. The transit profile is expected to be symmetric. The profile of the transit candidate does not exhibit significant departures from symmetry. This is another signal that the light curve shape is consistent with a transit.

Finally, we note that the shape of the sharp wall-like structures observed in many planetary transits is associated with the very small size of the planet relative to the star. When, however, the sizes of the planet and star are more similar to each other, the decline and subsequent recovery of the flux are more gradual. This is observed in Fig. 1 as it is, for example, in the transit of M dwarfs by hot Jupiters¹⁶.

Modelling the short-duration event as a transit

We model the intensity dip seen at $\sim 150\text{ ks}$ into the observation (Fig. 1) as an eclipse in which an opaque circular body obscures the XRS. We limit the time range of fit to a small interval around the dip so that the intensity of the XRS may be assumed to be constant. The events are binned at $\Delta t = 471.156\text{ s}$, corresponding to 150 times the charged couple device (CCD) readout duration (TIMEDEL = 3.14104 s), yielding an XRS intensity of $c_x \approx 7.5$ counts per bin. We carry out the fit using a method optimized to analyse low-count X-ray data explicitly using the Poisson likelihood, as it is appropriate in this regime. We use a Metropolis Markov chain Monte Carlo (MCMC) scheme to explore the model parameter space and find the optimal parameters, details of which are given in Methods ('Fits to the transit'). We then use the posterior probability densities of the parameters to evaluate the size of the eclipsing system. The radius of the circular XRS is R_x , and the

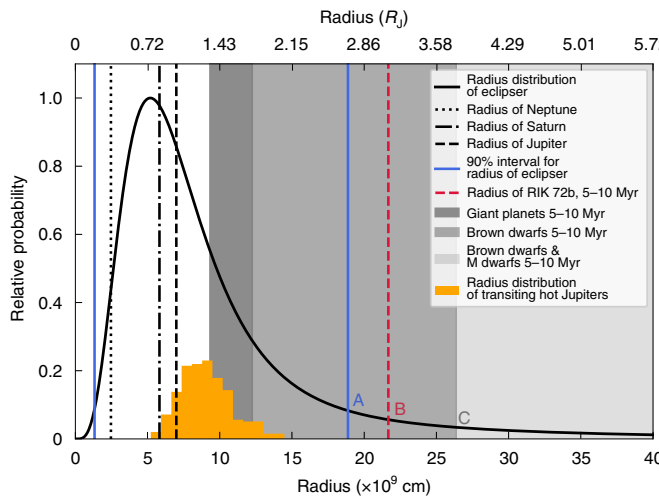


Fig. 5 | The probability distribution of transiting radii and the sizes of a variety of possible physical classes of transiter. The lower x axis is in units of 10^9 cm and the upper x axis is in units of Jupiter radii. The y axis represents the relative probability density for the radius of the eclipsor. The radius distribution of known transiting hot Jupiters is shown in orange. Several notable radius values are shown as vertical lines: the 90% highest posterior density (blue, with upper bound labelled 'A'); the radii of Neptune (dotted line), Saturn (dash-dotted line) and Jupiter (black dashed line); and the radius of the young brown dwarf within the Upper Scorpius association RIK 72b (red dashed line, labelled 'B'). The shaded regions represent the domains of radii of various young (5–10 Myr) populations¹⁷: giant planets (darkest grey shade), brown dwarfs (medium grey shade) and both brown dwarfs and M dwarfs (lightest grey shade, whose left edge is labelled 'C'). The integrated tail probabilities of the eclipsor having a larger radius than the radii marked A, B and C are $p(r > R_{A,B,C}) \approx 0.099, 0.075$ and 0.052 , respectively.

opaque circular eclipsor has radius $R_{\text{ec}} = f_{\text{ec}} \times R_x$. The light curve model is defined by five parameters:

$$\begin{aligned} \theta = & \{c_x, \text{baseline counts per bin}, \\ & T_{\text{mid}}, \text{midpoint of the eclipse}, \\ & b, \text{impact parameter}, \\ & f_{\text{ec}}, \text{eclipsor radius}, \\ & v_{\text{pl}}, \text{eclipsor velocity}\}. \end{aligned} \quad (1)$$

Times are expressed in units of kiloseconds from the beginning of the Chandra observation, and all distances are expressed in units of R_x ; thus, $b \times R_x$ is the smallest unsigned distance from the centre of the eclipsor to the centre of the source during the eclipse, and v_{pl} is computed in units of $\frac{R_x}{\Delta t}$. We use data in the range of $135 \text{ ks} \leq t \leq 165 \text{ ks}$ to construct the light curve; the eclipse occurs approximately between 145 ks and 158 ks.

The fit parameters are given in Table 1. Two features are particularly worthy of note. First, the value of the mode of the distribution of transiter radii is $f_{\text{ec}} = 0.74$, corresponding to a physical size comparable to Saturn's. Second, the mode of the relative speed between the transiter and the XRS is only 17 km s^{-1} . This indicates that the distance between the XRB and the transiting object is much larger than the radius of the inner binary (see 'The orbit of the transiting mass and its implications'). The probability distribution of transiter radii is shown in Fig. 5, supplemented by additional information about the physical radii of possible transitors. Extended Data Figs. 8–10 show, respectively, the model-derived nominal and cumulative

probability distributions of transiter radii, the marginalized posterior distributions of other fit parameters and several joint posterior distributions.

The nature of the transiting object

The black curve in Fig. 5 represents the probability distribution of transiter radii. Superposed is information about the galactic population of planets, brown dwarfs and M dwarfs. The radius distribution of roughly 300 transiting hot Jupiters is shown as an orange histogram, providing a comparison to planet-mass objects in an irradiated environment. These planetary radii fall within the 90% uncertainty interval of the probability distribution, but have a peak at about 1.4 Jupiter radii (R_J). From the solar system, we find Neptune below the mode and Saturn slightly above it, followed by Jupiter. There is a significant probability that the transiting object is smaller than Jupiter.

The red dashed line farther to the right corresponds to the radius of the young brown dwarf, RIK 72b. There is a chance of only 0.075 that the eclipsor is this large or larger. The grey bars indicate the ranges of sizes predicted by models¹⁷ for brown dwarfs and M dwarfs as functions of age. As the example of RIK 72b illustrates, the probabilities of large-radius transitors are small. In addition, large radius solutions are deprecated because they require a strong coincidence with the distance of closest approach—for $R_{\text{ec}} > 3 R_J$, a narrow band of progressively larger b are allowed—which is a property of the observer viewing geometry and unrelated to the system (see discussion in 'Fits to the transit'). Essentially, independent of the low calculated probability of large R_{ec} , a large eclipsor can produce a short-lived transit only for an increasingly limited range of approaches, requiring more fine-tuning.

Only planets and white dwarfs have equilibrium radii that span the full range of likely transiter radii. We can, however, eliminate white dwarfs from consideration because, in the expected range of distances from the XRS, a white dwarf would serve as a gravitational lens, increasing the amount of light we receive from the XRS rather than causing a dip (Methods).

Furthermore, white dwarfs can form only when the low-to-intermediate-mass stars producing them have evolved, generally at ages greater than 10^8 yr. The estimated age of the counterpart to M51-ULS-1 is roughly 50 times smaller. Also supporting the youth of M51-ULS-1 is its position on the edge of a star-forming cluster and its nature as a high-mass extragalactic ultraluminous XRS, whose donor stars tend to be similar in age to the likely counterpart. The youth of the XRB also serves to make it highly unlikely that the transiter is either a brown dwarf or an M dwarf. Members of each of these two classes are born with radii larger than our 90% limit.

We nevertheless carefully consider both M dwarfs (stars with mass less than about $0.5 M_\odot$) and brown dwarfs. For M dwarfs, only those of lowest mass can shrink enough to be consistent with the 90% limit, and adequate shrinkage even for these requires longer times than can be accommodated by the age of M51-ULS-1. The radius of a $0.1 M_\odot$ ($0.2 M_\odot$) M dwarf takes roughly 50 Myr (100 Myr) to decrease to $2 R_J$. Beyond that, M dwarf radii tend to be 5–10% larger than predicted by theory, and can be 'inflated' by up to 50% (ref. ¹⁸), even for stars older than 100 Myr.

Brown dwarfs have masses between $13 M_J$ and $80 M_J$. They are born with relatively large radii (5.4 – $1.8 R_J$ at ages of 5–10 Myr) and shrink with age (3.7 – $1.4 R_J$ at ages of 10–50 Myr). In addition, brown dwarfs are rare relative to planets, a phenomenon known as the 'brown dwarf desert' (Fig. 6)^{19,20}.

Although the youth of the M51-ULS-1 alone serves to indicate that M dwarfs and brown dwarfs are too large, we note in addition that the ULX's high luminosity may also lead to bloating and can increase the time needed to shrink to equilibrium. The orbital

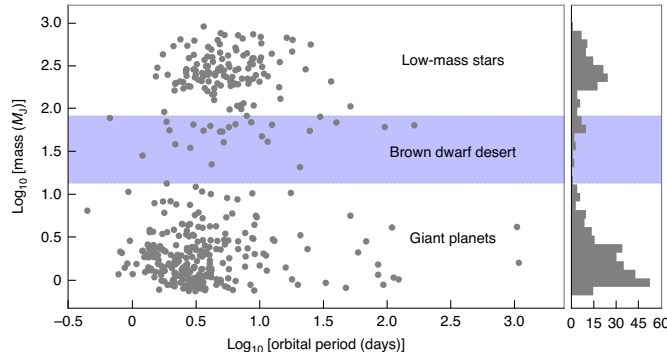


Fig. 6 | Mass-period distribution of a sample of low-mass stellar companions, all known transiting brown dwarfs, and a sample of the transiting giant planet population. The population of brown dwarfs (shown via the horizontal blue band) is exaggerated here in that all known transiting brown dwarfs are shown, whereas only a sample of the giant planet population (courtesy of <http://www.exoplanet.eu>) and a sample of the low-mass stellar companion population¹⁹ are shown. The right-hand panel shows the mass distribution of objects across the $0.5 M_{\odot}$ ($4.8 \times 10^{-4} M_{\odot}$) to $300 M_{\odot}$ ($0.29 M_{\odot}$) mass range.

separation between the XRB and transiter is likely in the range of tens of astronomical units (see ‘The orbit of the transiting mass and its implications’). At this distance, the incoming flux can be comparable to the flux received by a ‘hot Jupiter’ from a Sun-like star. Whether the flux is significantly larger or smaller depends on its exact distance from the centre of mass of the XRB, which we can only estimate based on the relative velocity derived in Methods (‘Fits to the transit’) and shown in Table 1. One difference between the incident flux and the influxes to low-mass objects generally simulated in the literature is that M51-ULS-1 is a copious emitter of X-ray and extreme ultraviolet radiation. We can gain insight from a number of investigations that consider the effects of comparable received flux on planetary atmospheres, some even considering stars with energy output at ultraviolet or X-ray wavelengths^{21,22}. The circumstances under which planetary and brown-dwarf atmospheres are ablated by irradiation is still, however, under active consideration. The transiter in M51-ULS-1 shows no signs of ablation, which would likely alter the eclipse profile and introduce energy dependence detectable through a change in hardness ratio.

To provide additional context, we extracted systems from the <http://www.exoplanet.eu> site, identifying all exoplanets older than 2 Myr and younger than 10^8 yr and with orbital separations between 10 au and 1,000 au. The catalogue includes brown dwarfs as well as planets. We searched for all objects with estimated masses $< 70 M_{\oplus}$, and with estimated radii $< 10 R_{\oplus}$. Seven objects have masses firmly in the range of Jupiter-class planets. Their ages range from 4.5 Myr to 26 Myr and their radii range from $1.1 R_{\oplus}$ to $2.5 R_{\oplus}$. The system with the largest radius is ROXs 428 (AB)b, one of the youngest systems at $(6.8 + 3.4 - 2.3)$ Myr. The host star has a mass of only $0.6 M_{\odot}$, and the planet is 140 au from it. In this case, irradiation is unlikely to play a role, so the large size of the planet is likely associated with the system’s young age.

It is worth noting that all of the radii are larger than $1.1 R_{\oplus}$. Furthermore, even in the absence of large incident flux, there is a tendency for the younger, more massive objects to be somewhat larger.

The orbit of the transiting mass and its implications

If we assume the transiting object to be a planet, we can calculate its orbit and related properties. Milky Way planets not orbiting the Sun are referred to as exoplanets and each is given the name

Table 1 | Results from the MCMC analysis

Parameter	Mode	90% bounds ^a	Mean $\pm 1\sigma$
c_x (counts per bin)	7.6	(7.3, 8.0)	7.6 ± 0.2
b (km)	0	$(0, 1.8 \times 10^5)$	$(7 \pm 11) \times 10^4$
$f_{ec}(R_{\oplus})$	0.74	(0.18, 2.7)	1.4 ± 1.3
v_{pl} (km s^{-1})	17.1	(5.1, 56)	30 ± 20
T_{mid} (ks)	152.7	(152.2, 153.4)	152.8 ± 0.4
^b Eclipse start (ks)	147.8	(143.9, 151.3)	147.4 ± 2.6
^b Eclipse duration (ks)	10.5	(3.1, 17.9)	11 ± 5

^a Highest posterior density bounds. ^b These are values computed from model parameters, not fitted directly.

of the star it orbits, with a lower-case subscript. The object transiting M51-ULS-1 is not only outside the Solar System, but also far outside the Galaxy. It is an extragalactic planet-size object orbiting a well-defined binary system. We refer to the transiter as a possible ‘extroplanet’, M51-1 (M51-ULS-1).

It is straightforward to determine the value of a_{pl} , the distance of M51-ULS-1’s extroplanet from the binary’s centre of mass at the time of transit, as the value of v_{pl} was measured from the short-eclipse fit. The most likely value of v_{pl} , the mode of the distribution, is 17 km s^{-1} , and the 68% uncertainty bounds are at 8 km s^{-1} and 34 km s^{-1} .

Kepler’s law demands that a_{pl} scale as M_{tot}/v_{pl}^2 , as long as the transiter’s mass is much smaller than the mass of the binary.

$$a_{pl} = 45 \text{ au} \left(\frac{M_{\text{tot}}}{20 M_{\odot}} \right) \left(\frac{20 \text{ km s}^{-1}}{v_{pl}} \right)^2. \quad (2)$$

As such, the distance between the candidate planet and the centre of mass of the XRB is in the range of tens of astronomical units.

Although we must be careful not to over-interpret the specific values in Eq. (2), the important point about the range of possible values is that they tend to be significantly larger than the radius of the inner orbit. As long as the ratio between the outer and inner semimajor axes is larger than about 3, the triple is dynamically stable and the transiter is in a circumbinary orbit.

The luminosity of M51-ULS-1 is roughly 10^6 times that of the Sun. The flux received by a planet tens of astronomical units from the ULX is comparable to the flux received by a ‘hot Jupiter’, which might be hundredths of an astronomical unit from a solar-type star.

The high effective temperature of the XRS ($\sim 10^6$ K) means not only that it is a copious emitter of X-rays, but also that a large fraction of the radiation it emits is highly ionizing. Such radiation can lead to the loss of the planetary atmosphere. Although highly luminous systems such as M51-ULS-1 have not yet been considered as planetary hosts, an analogous case has been studied²³. Close-in circumbinary planets around tidally locked cool stars, which tend to have more active coronae, are expected to be strongly affected by photo-evaporation.

At the orbital distance we have estimated for M51-1 (M51-ULX-1), its atmosphere is likely to survive the presently observed X-ray active phase of M51-ULS-1. As the field of planets in XRBs develops, we may find that gas and ice giants do not survive the ultraviolet flux in the spatial region occupied by the candidate extroplanet M51-1 (M51-ULS-1), placing upper bounds on the radius of the transiter. At optical and infrared wavelengths the dominant source of flux may be the donor star, although the magnitude of the HST-discovered counterpart suggests that the donor

does not have a higher bolometric luminosity than the XRS. Thus, the discussion above will not be significantly altered by including the effects of the donor star. We note, however, that candidate exoplanet M51-1 (M51-ULS-1) is indeed influenced by the large total incident radiation. In an analogy to close-orbit exoplanets it would likely experience bloating, having a radius somewhat larger than expected for an object of the same mass and age in a less hostile environment.

Galactic populations of planets and prospects for future observations

There is no reason to expect that the data sets we employed are extraordinary. We therefore examined archived data to determine how many independent and roughly equivalent studies could be conducted, to explore the prospects for future discoveries with either XMM-Newton or Chandra.

A search of the Chandra archive found that at least seven galaxies have been observed for 750–1,500 ks and 13 others for 250–500 ks. Two of the best observed galaxies, M31 and M33, are members of the Local Group, where sources ten to a hundred times less luminous than the ones we have studied provide enough photons to allow the detection of short transits. Data from dozens of other galaxies with shorter observations are also useful. XMM-Newton's archives are comparably rich.

We therefore anticipate the discovery of more extragalactic candidate planets in wide orbits. Furthermore, additional data from external galaxies are collected every year. Below we discuss how existing data can also be used to search for planets with closer orbits and for planets orbiting dimmer XRBs.

The reason external galaxies are good places to hunt for planets is that the field of view of today's X-ray telescopes encompass a large fraction of the bright portions of galaxies at distances larger than 6–7 Mpc. This means that a single observations can collect counts from dozens to hundreds of XRSs. As we consider galaxies nearer to us, the advantage of a broad field of view is diminished. There is nevertheless a significant advantage to be gained because, for example, at the distance to M31 we collect ~100 times as many counts as we would from the same XRS in a galaxy at 8 Mpc. In addition, for bright sources, this makes us sensitive to shorter-lived deviations from baseline. Thus, small planets in orbits such as that of exoplanet M51-1 (M51-ULS-1) can be detected, and planets in closer orbits can be detected as well. Furthermore, as the numbers of XRSs at lower luminosities is larger than the number of high-luminosity sources, planet searches can be conducted on the much larger populations of dimmer XRBs. For example, the central region of M31 contains roughly 400 XRSs with total observing times longer than 0.5 Ms, most with luminosities between 10^{36} erg s $^{-1}$ and 10^{38} erg s $^{-1}$. At lower luminosities substellar objects may be able to survive for longer times in smaller orbits. We will be able to either discover such planets or place meaningful limits on their existence.

Finally, the closest XRSs to us are in our own Galaxy, where even light curves of white dwarfs that accrete from close companions at low rates (cataclysmic variables), with luminosities on the order of 10^{31} erg s $^{-1}$, can be examined for evidence of transits. Unless, however, the target is a stellar cluster or other crowded field, only one XRS may be in a single field of view. Furthermore, long exposures are available for smaller numbers of XRSs than in external galaxies. Nevertheless, some XRSs have had excellent time coverage by, for example, the past X-ray mission Rossi-XTE or by the current NuSTAR, NICER and eROSITA missions. In addition, new missions, such as Athena and the proposed Lynx mission, will increase the X-ray count rates significantly, making it possible to discover more planets in all of the environments considered above.

Once we have developed a larger sample size, we will be able to answer some physical questions about planets orbiting XRBs in other galaxies, as well as those orbiting XRBs in the Milky Way.

For example, we will know if planetary transits are found primarily around the XRBs that we observe to be eclipsing, establishing the frequency of aligned orbits. We will find planets with a range of sizes and with a range of orbital radii, and will explore the relationship between planet properties and host XRB characteristics. We will determine features associated with any false positives. We can then use general expressions for the detection probability to extrapolate from our discovered sample of planets to the size and characteristics of the underlying populations in the galaxies we study (Methods, 'Probability of detecting a transit or a transition to eclipse').

Discussion

The discovery of a possible planet in an external galaxy required a combination of theoretical work, the capabilities of the present generation of X-ray observatories, and a collaboration among X-ray astronomers and experts on binaries, stars, brown dwarfs and planets. This work demonstrates a new method with the potential to discover planets in a wide range of systems hosting XRSs. Because the most luminous XRSs can be detected in external galaxies, the search for exoplanets, planets in orbits located outside the Milky Way, has now become a realistic and practical enterprise.

Methods

The X-ray observations. *Chandra.* Between 2000 and 2018, M51 was observed with Chandra's Advanced CCD Imaging Spectrometer (ACIS) a total of 16 times. Two of these observations were too short (<2 ks) for meaningful timing analysis and thus were ignored. We used the remaining 14 observations, which are summarized in the Extended Data Fig. 1 table of observations. Data were downloaded from the public archive and reprocessed using standard tasks in the Chandra Interactive Analysis of Observations (CIAO) software package, version 4.11 (ref. ²⁴). For each observation, we found the count rate of M51-ULS-1. To take into account the declining sensitivity of the ACIS-S detector, particularly in the soft band, all count rates were converted to their Cycle 12 equivalent using the online tool PIMMS version 4.9. The corrected count rates are displayed in Extended Data Fig. 2. We extracted light curves using circular regions of ~4 arcsec, centred on M51-ULS-1, with nearby background regions at least three times as large. The 'dmextract' tool was used to create background-subtracted light curves, and analysis was performed using the FTOOLS task ²⁵ 'lcurve'.

We used the spectral fitting performed by Urquhart and Soria⁷ and reported in their Table 2 for constraints on the size of the X-ray emitting region. For full details of the spectral analysis, see ref. ⁷.

XMM-Newton. Of the 13 publicly available XMM-Newton observations of M51, three observations excluded data-taking because strong background flaring occurred. We downloaded the ten remaining observations from NASA's High Energy Astrophysics Science Archive Research Center (HEASARC). We reprocessed the European Photon Imaging Camera (EPIC) observations using standard tasks in the Science Analysis System (SAS) version 18.0.0 software package. Intervals of high particle background exposure were filtered out. Standard flagging routines #XMMEA_EP and #XMMEA_EM (along with FLAG=0) and patterns 0–4 and 0–12 were selected for pn and metal oxide semiconductor camera, respectively. As with the Chandra data, we extracted the count rates of M51-ULS-1 for each observation, before converting them to their Chandra Cycle 12 equivalent using the PIMMS tool. Light curves were extracted from circular regions with radii of 20 arcsec, with local background regions selected to be at least three times larger. We used the SAS tasks 'evselect' and 'epiclccorr' to create background-subtracted EPIC-combined light curves. The observations and corrected count rates are displayed in tabular form in Extended Data Figs. 1 and 2, respectively.

Finally, we note that we have established that the dip is not due to a loss of telemetry by checking the signal from nearby XRSs as well as the counts from the full field of view. Light curves from several XRBs observed at the time of the transit-like event are shown in Extended Data Fig. 3.

Search for X-ray transits. *Identifying transits.* We conducted a systematic search for possible transits in the Chandra X-ray light curves of XRSs in three galaxies: M51 (a face-on interacting late-type galaxy), M101 (a face-on late-type galaxy) and M104 (an edge-on early-type galaxy with some star formation). These light curves were available because they had recently been studied for other purposes^{26,27}. It is possible to make discoveries of planetary transits in archived X-ray light curves, because short-term time variability was often not a primary focus of the original observing programmes. Even relatively long-lasting stellar eclipses lasting ten or more hours have been found after the initial analyses were complete²⁶. Planetary transits, a phenomenon that has apparently not been previously targeted, exhibit short-duration deficits of photons and are therefore particularly prone to being missed or misidentified.

We considered all observations of duration greater than 5 ks, and all ObsIDs (individual observations) for each XRS observed to have had a flux corresponding to $L_x(0.5\text{ keV} - 8\text{ keV}) > 10^{37}\text{ erg s}^{-1}$ during at least one observation. We studied 667 light curves produced by 55 XRSs in M51, 1,600 light curves from 64 XRSs in M101 and 357 light curves from 119 XRSs in M104. The numbers of light curves are larger than the total numbers of XRSs because each physical source was in the fields of multiple exposures. We conducted an automated search specifically designed to identify transits. We required only that there be at least one 1 ks interval with no X-ray counts, and that, however long the low state lasted, there should be a baseline with roughly equal count rates prior to and after the downward dip. We applied our search algorithm to all 2,624 light curves in the sets described above.

The criteria, that the light curve should exhibit a drop to zero measured count rate in at least one 1 ks bin, and that the downward deviation should start from and return to a baseline, were enforced as follows. Considering an individual light curve, and denoting the counts in bin i as $C(i)$, we identified all values of i for which $C(i)=0$. We then considered the time bins just before i ($C(i-j), j=1, 2, \dots$) and just after ($C(i+j), j=1, 2, \dots$). The purpose of this was to measure the duration of the interval during which the count rate was consistent with zero. We did this by counting the total number of consecutive bins in which the count rate was equal to or smaller than 1. The first and last of these bins were, respectively, i_{low} and i_{high} , so the duration of the low state is $[(i_{\text{high}} - i_{\text{low}}) + 1]$ ks. To determine whether the low state corresponds to a transit, we needed to establish whether the dip started from and returned to a baseline. We therefore considered, in turn, four pairs of points, $(C_1 = C(i_{\text{low}} - k), C_2 = C(i_{\text{high}} + k))$, for which the value of k ranges from 1 to 4. For each of the four pairs we defined $\sigma = \sqrt{\max(C_1, C_2)}$. If the absolute value of the difference between C_1 and C_2 was less than 2σ , we considered that pair to be a match. We also required that both C_1 and C_2 be 7 or larger, to ensure that the count rate at baseline is significantly higher than it would have been during the low-count-rate interval. We conducted this check for four pairs of points ($k=1, 2, 3$ and 4). If at least two of the four pairs had high enough count rates and were also matches, we considered the event to be a possible transit and flagged it for visual inspection. The 2,624 light curves in our study yielded one interval for inspection. This was the light curve in Fig. 1, with an apparent transit lasting 10 ks to 12 ks. Extended Data Fig. 3 shows high-count-rate sources detected in the Chandra observation that included the transit event.

We also employed other approaches to study the light curves. For each of the 2,624 light curves, we plotted the cumulative count rate by using a method developed by Irwin et al.²⁸ to discover flares in XRSs. We tested the method to determine whether it could also discover dips, and found it to be effective. The signature of an eclipse, for example, is a flat region in the plot of cumulative count rate versus time.

We also measured the total number of counts in each exposure, C , and used C/T_{exp} , where T_{exp} is the exposure time, to compute the average count rate. We computed running averages of the counts per kilosecond, located the positions of local extrema and binned the data, initially selecting the bin size so that there would be an average of 10 counts per bin. We subsequently conducted a visual inspection of each light curve with $C > 100$ to look for dips in flux. We compared the results of our algorithmic analyses (for example, significance of changes in flux) with visually identifiable features in the light curve. This process led to the selection of the event shown in Fig. 1.

The identification of a single transit candidate in our thorough search through the Chandra light curves of M51, M101 and M104 demonstrates both that transits can be found and that transit profiles are not common features of the light curves of extragalactic XRSs. Criteria that are less strict (for example, not requiring a drop to zero flux) might have identified more candidates; our goal, however, was to identify only strong candidates that could then be subjected to the sequence of further tests we carried out.

Evidence for stellar eclipses. Two observations, one by Chandra and one by XMM-Newton, exhibit a transition from a low to a high state and from a high to a low state, respectively. In each case, the transition occurred during an interval of a kilosecond. The variation shown in the lower panel of Extended Data Fig. 6 exhibits behaviour consistent with an egress from an eclipse, presumably by the donor star. The low state is consistent with zero flux. This state begins prior to the start of the exposure and continues for 15 ks; the duration of the observed portion of the low state is longer than the full duration of the transit event we present in this paper. A change in hardness ratio would likely signal a change in state, whereas during an eclipse the decrease in flux from the harder and softer X-rays occurs at roughly the same time. In sharp contrast to the transiter producing the dip in Fig. 1, the eclipsor is significantly larger than the XRS.

The upper panel of Extended Data Fig. 6 shows what appears to be an ingress to eclipse, as observed by XMM-Newton. There is a sharp decline as expected for ingress. There is, however, residual emission that shows some spectral variation detectable even during the low state. XMM-Newton's point spread function is large, including X-ray emission from sources within a few tens of parsec at the distance to M51. We have examined the Chandra images of M51-ULS-1 and its surroundings and found several (fainter) point-like XRSs and diffuse emission inside the XMM-Newton/EPIC source extraction region (Extended Data Fig. 7).

It is therefore reasonable to hypothesize that the low state is a full eclipse, and that the faint residual emission seen during that time interval in the XMM-Newton data comes from those other sources unresolved by XMM-Newton.

The Chandra-observed transition from a low state is an excellent candidate for an eclipse egress, and the XMM-Newton-observed transition from a low state is a good candidate for an eclipse ingress. The significance of detecting an ingress to or egress from a stellar eclipse is that it tells us that our line of sight is roughly aligned with the orbital plane. In the section 'Probability of detecting a transit or a transition to/eclipse' we will show that the probability of an ingress and/or egress occurring during the roughly 1 Ms of observations afforded M51-ULS-1 may be close to unity. The X-ray light curve exhibits evidence of eclipses by the donor star, as shown in Extended Data Figs. 6 and 7. The occurrence of stellar eclipses is not directly related to the identification, analysis or interpretation of the apparent transit. The eclipse does place some constraints on the orientation of our line of sight relative to the orbital plane. The angular deviation is constrained by the ratio R_d/a_b , where R_d is the radius of the donor and a_b is the radius of the binary orbit.

Fits to the transit.

For planar circles whose centres are separated by a distance

$$d(t) = \sqrt{b^2 + (|t - T_{\text{mid}}| v_{\text{pl}})^2}, \quad (3)$$

we compute the area of overlap $A(t)$ at time t between the foreground object and the XRS,

$$\begin{aligned} A(t) &= 0 \quad \text{for } d(t) > 1 + f_{\text{ec}} \\ &= \pi \quad \text{for } \max\{1, f_{\text{ec}}\} > d(t) + \min\{1, f_{\text{ec}}\} \\ &= (\alpha_X - \cos \alpha_X \sin \alpha_X) \\ &\quad + f_{\text{ec}}^2 (\alpha_{\text{ec}} - \cos \alpha_{\text{ec}} \sin \alpha_{\text{ec}}) \quad \text{otherwise,} \end{aligned} \quad (4)$$

where α_X and α_{ec} are the angles subtended by the intersecting arcs of the star and the foreground object, respectively:

$$\begin{aligned} \alpha_X &= \arccos \frac{d(t)^2 + 1 - f_{\text{ec}}^2}{2 d(t)} \\ \alpha_{\text{ec}} &= \arccos \frac{d(t)^2 + f_{\text{ec}}^2 - 1}{2 d(t) f_{\text{ec}}}. \end{aligned} \quad (5)$$

Note that when the source and eclipsor are of the same size ($f_{\text{ec}}=1$) and perfectly aligned (impact parameter $b=0$), then $\alpha_X = \alpha_{\text{ec}} = \arccos \frac{d(t)}{2}$, resulting in $A=\pi$ at $d(T_{\text{mid}})=0$ (complete overlap at the midpoint of the eclipse). The Methods describe the fits in more detail. Summaries of the estimated parameter values are given in Table 1.

Here we describe the MCMC-based fitting²⁹ that we carry out to estimate the parameters of the eclipse light curve model described in 'Modelling the short-duration event as a transit'. We use a Metropolis scheme in which new parameter values are drawn based on their current values; we employ as proposed distributions a Gaussian for c_X and T_{mid} , uniform for b and uniform in \log for f_{ec} and v_{pl} . We further restrict

$$\begin{aligned} 0 &< c_X \text{ (counts per bin)} < \infty, \\ 145 &\leq T_{\text{mid}} \text{ (ks)} \leq 158, \\ 0 &\leq f_{\text{ec}} (R_X) \leq 50, \\ 0 &\leq b (R_X) \leq 51, \\ 10^{-3} &\leq v_{\text{pl}} \frac{R_X}{0.471156 \text{ ks}} \leq 10. \end{aligned} \quad (6)$$

We do not explicitly tie together f_{ec} and b , although the fact that an eclipse is observed requires that $b < (f_{\text{ec}} + 1)$; we expect this correlation to be recovered from the MCMC draws. We also sample the background level in each iteration from a Gaussian distribution, background $\approx N(0.38, 0.018^2)$ to account for uncertainty in background determination. We compute the Poisson likelihood of the observed light curve counts for each realization of a model light curve for the parameter values drawn in that iteration, and accept or reject the parameter draw based on the Metropolis rule (always accept if the likelihood is increased, otherwise accept with probability equal to the ratio of the new to old likelihoods).

We first run the MCMC chain for 10^5 iterations using a starting point of $\theta^{(0)} = \{c_X = 7.75, b = 0.5, f_{\text{ec}} = 2.0, v_{\text{pl}} = 0.9, T_{\text{mid}} = 150\}$. We sample 40 different starting points as random deviates from the resulting posterior distributions, and again run 10^5 iterations for each case. The first 2,000 iterations are discarded as burn-in in each case. We combine all the iterations after verifying that the chains converge to the same levels for all parameters. We then construct posterior probability distributions for each parameter as histograms from the MCMC draws after thinning them to the effective sample size ($N_{\text{eff}} = \frac{1-\rho}{1+\rho}$, where ρ is the lag 1 correlation) in 5,000 iteration increments.

How good is the resulting model fit? Unlike with χ^2 fitting, a simple measure of a model goodness-of-fit criterion does not exist for Poisson likelihood-based fits.

However, a consideration of the Poisson equivalent of the χ^2 , the cstat statistic³⁰, allows us to obtain a reasonable estimate. The measured cstat for the best-fit model light curve is 33.3, and is well covered by the expected cstat based on a null distribution of 33 ± 8 . We thus conclude that the light curve model of Eq. (4), with the parameters set out in Table 1, is a good fit to the data.

We convert the relative units of b , f_{ec} and v_{pl} to physical units by convolving the MCMC posterior draws with a representative distribution of $p(R_{\text{x}})$ derived from the X-ray data. As noted above, the 90% bounds on R_{x} are asymmetric, at $[-1.1, +4.1] \times 10^9 \text{ cm}$ from the nominal best-fit value of $2.5 \times 10^9 \text{ cm}$. This can be represented by half-Gaussians with widths appropriate for the corresponding 90% bounds (note that for a standard Gaussian distribution, 90% of the area on one side of the mean is covered at $\pm 1.95\sigma$), which are then rescaled to be continuous through the best-fit value, which now represents the mode of the pasted Gaussian (see the red and blue dashed curves in the left panel of Extended Data Fig. 8). However, such rescaling, although it preserves the location of the mode, makes the overall distribution narrower, and the resulting 90% bounds are no longer consistent with the observed values (see intersections of the dashed red and blue cumulative distribution with the horizontal dotted lines at 5% and 95% levels, in the right panel of Extended Data Fig. 8). We therefore adopt a gamma distribution (solid green lines in Extended Data Fig. 8) as the representative distribution for R_{x} . Specifically, we choose $\gamma(R_{\text{x}}; \alpha = 5.36, \beta = 1.45)$; the peak here is displaced by $\sim 20\%$, but we consider this a better representation of R_{x} because it matches the measured bounds of R_{x} at the 5% and 95% levels well.

The distributions of the various parameters are shown in Extended Data Figs. 9 and 10. The envelope of the ensemble of models that fall within the 68% highest-posterior-density intervals for each parameter are shown in Extended Data Fig. 9. In each case, the location of the mode (vertical solid orange line), the 68% (blue dashed vertical lines) and 90% (green dashed vertical lines) highest-posterior-density intervals, and the mean and 1σ errors (horizontal red line situated at the same vertical level as peak of the distribution) are marked. Note that in several cases the distributions are skewed, and traditional estimates such as the mean and standard deviation are not useful summaries. We thus also provide the mode of the distribution and the 90% highest-posterior-density intervals (these are intervals that enclose the highest values of the posterior probability density, and are consequently the smallest uncertainty intervals that can be set). There are also strong correlations present between b , f_{ec} and v_{pl} as seen from the contour plots of their joint posteriors (constructed without thinning the iterations). This suggests that the intervals derived from the marginalized one-dimensional posteriors are too coarse, and that narrower intervals may be obtained over smaller ranges. For instance, $v_{\text{pl}} > 40 \text{ km s}^{-1}$ are predominantly obtained when $f_{\text{ec}} > 2 R_{\text{j}}$, which itself has a lowered probability of explaining the data. Thus, the preponderance of the probability suggests that the system is better described with smaller values of f_{ec} and v_{pl} . Furthermore, note that b and f_{ec} have a large and narrow extension to large values; this can occur essentially because an eclipse can occur for large b only when f_{ec} is also large enough to cover the source even at large displacements. That is, the space of possible models that allow this situation are predominantly driven solely by the depth of the eclipse and not the profile. Solutions that involve $R_{\text{ec}} < 2 R_{\text{j}}$ would be plausible over a large range of observer viewing angles (Extended Data Fig. 10, top panel), but for $R_{\text{ec}} \gg 3 R_{\text{j}}$, only a narrow band of progressively larger b values are allowed. In other words, the allowed solutions occupy a narrow part of the available parameter space (<10% of the available range of b for any given $R_{\text{ec}} > 3 R_{\text{j}}$), which is effectively a low-entropic scenario. Our model allows such solutions to be found, as the corresponding model light curves are consistent with the observed light curve but requires extreme coincidences of viewing geometry that are implausible. This consideration is independent of, and supplements, the low probabilities of R_{ec} and b illustrated in Extended Data Fig. 10. A measure of this implausibility is not included in our model as such a condition cannot be imposed a priori.

Feasibility of wide orbits. We know that the existence of planets in wide orbits is plausible, because planets with orbits having semimajor axes in the range of tens and hundreds of astronomical units are common among Galactic exoplanets. Direct imaging has led to the discovery of 15 confirmed exoplanets with estimated mass smaller than $13 M_{\oplus}$ and semimajor axes between 10 au and 100 au; similarly, 12 exoplanets have semimajor axes wider than 100 au (<http://www.exoplanet.eu>; 2020 July 9). There is also a case of a planet in a 23 au orbit about a former XRB in M4 (ref. ³¹).

Even without a detailed evolutionary model, we know that the binary M51-ULS-1 had an interesting history. Here we discuss key elements of that history and show that a wide-orbit planet could survive. M51-ULS-1 experienced an earlier phase of activity during which the star that evolved into today's compact accretor was active. This star could have transferred mass to its companion. However, less accretion energy would have been released per unit mass than is released today because the companion was not compact. The evolution of the most massive star would, however, have had consequences for a circumbinary planet. The evolving star would become more luminous and larger. It would also shed mass through winds, which would tend to make the planetary orbit wider. If a significant amount of mass was ejected in the orbital plane, the planet's orbit would likely have been driven towards the midplane. It is important to note that, even if the first-evolved star reached giant dimensions, a planet in an orbit that was

initially several astronomical units wide would be able to survive and would likely be pushed into a wider orbit. If the present-day compact object is a black hole, the formation event may have been a 'failed supernova' during which relatively little mass was lost. If instead the present-day compact object is a neutron star, significant mass may have been lost through a supernova, and there may also have been a 'kick'. Nevertheless, the presence of the massive star that is today's donor would have allowed the system to survive and would have moderated the speed of the neutron star's natal kick. Just as it is possible for a binary to survive a supernova explosion, it is also possible for wide-orbit planets to stay bound.

We note that, should a planet or brown dwarf have experienced an epoch of proximity to the binary accretor, the intense radiation could have ablated its gaseous atmosphere, leaving behind a less massive and smaller solid core. A planet with radius near or below the mode could therefore be either a naturally formed terrestrial planet or the core of a planet that once had a large atmosphere.

The bottom line is that the wide orbit we derive is consistent with the existence and survival of the planet, both in the presently observed binary and through the possible evolution of the primordial binary, even though not every planet hosted by the XRB will have the same fate.

Gravitational lensing: exoplanet M51-1 is not a white dwarf. White dwarfs can be eliminated as possible transits of M51-ULS-1 because of the binary's youth. Here we show that there is another reason, based on the physics of gravitational lensing, to rule out the possibility that exoplanet M51-1 (M51-ULS-1) is a white dwarf. In the range of derived orbits (approximately tens of astronomical units), a white dwarf would act as a gravitational lens, increasing the amount of light we receive from the XRS, not decreasing it. The gravitational influence of a mass deflects light passing near it. When a mass is dense enough to fit within a radius known as its Einstein radius, its effect on the light reaching us from a distant point source is to increase the amount of light we see, rather than to cause a dimming³¹. The value of an object's Einstein radius depends on its mass and on our distance to the lens and source. In the case we consider, the lens (that is, the white dwarf) and light source (that is, the XRS) are separated by a much smaller distance than the distance to the observer. Only the distance, a , between the two of them plays a significant role. The expression for the Einstein radius is

$$R_E = 1.16 \times 10^{10} \text{ cm} \left(\frac{M}{M_{\odot}} \right)^{\frac{1}{2}} \left(\frac{a}{15 \text{ au}} \right)^{\frac{1}{2}}. \quad (7)$$

Thus, any white dwarf in the orbital range derived for exoplanet M51-1 (M51-ULS-1) would fit inside its Einstein ring. It would therefore serve as a gravitational lens, increasing the number of X-rays we would detect during its passage across the XRS. It is therefore not possible that the decrease in flux observed during the transit event was caused by the passage of a white dwarf.

Probability of detecting a transit or a transition to eclipse. The probability of detection, \mathbb{P} , is the product of a temporal factor \mathcal{P} and a spatial factor \mathcal{F} :

$$\mathbb{P} = \mathcal{P} \times \mathcal{F}. \quad (8)$$

Regarding the temporal factor, both planetary transits and transitions to stellar eclipse (an ingress or an egress) are short-lived events whose durations are many times smaller than that of typical exposures of M51. Let T_{obs} be the total time duration of exposures and P_{orb} be the orbital period:

$$\mathcal{P} = \min \left[\frac{T_{\text{obs}}}{P_{\text{orb}}}, 1 \right]. \quad (9)$$

If T_{obs} is longer than N orbital periods, then $\mathcal{P} = 1$ and, on average, N ingresses and egresses will be observed. Observations of M51-ULS-1 lasted for a total of $\sim 1 \text{ Ms} \approx 11.6 \text{ d}$; this is the value of T_{obs} .

Regarding the spatial factor, an eclipse or transit can be detected only if the orbital plane is approximately aligned with our line of sight. The probability is

$$\mathcal{F} = \frac{(R_{\text{x}} + R_{\text{ec}})}{a_{\text{orb}}}, \quad (10)$$

where R_{x} is the radius of the XRS and R_{ec} is the radius of the eclipsor.

Ingress to or egress from stellar eclipse. The orbital period can be expressed as follows:

$$P_{\text{bin}} = 9.6 d \left[\frac{a_{\text{bin}}}{50 R_{\odot}} \right]^{\frac{3}{2}} \left[\frac{20 M_{\odot}}{M_{\text{tot}}} \right]^{\frac{1}{2}}. \quad (11)$$

Thus, the temporal factor determining the probability of detecting an ingress or an egress is

$$\mathcal{P}_{\text{in-eg}} = \min \left[1.2 \left[\frac{T_{\text{obs}}}{1 \text{ Ms}} \right] \left[\frac{50 R_{\odot}}{a_{\text{bin}}} \right]^{\frac{3}{2}} \left[\frac{M_{\text{tot}}}{20 M_{\odot}} \right]^{\frac{1}{2}}, 1 \right]. \quad (12)$$

Although we don't know the exact values of a_{orb} or M_{tot} , the above equation shows that, for values consistent with expectations of the size of the binary's orbit and total mass, the value of $\mathcal{P}_{\text{in-eg}}$ can be near unity.

In the case of a stellar eclipse, $R_x < R_{\text{ec}}$. This is why an ingress (or egress) exhibits a sharp fall (or rise). As the eclipsor is the donor star, we have $R_{\text{ec}} = R_d$. The easiest case to consider is that in which the donor fills its Roche lobe, yielding $a_{\text{bin}} = R_L/f(q)$, where $q = M_d/M_a$, M_a is the mass of the accretor, and $f(q)$ is given by³²

$$f(q) = \frac{0.49 q^{\frac{2}{3}}}{0.6 q^{\frac{2}{3}} + \ln(1 + q^{\frac{1}{3}})}. \quad (13)$$

$R_L = R_d$, where R_L is the effective radius of the Roche lobe. Roche-lobe filling implies that $a_{\text{bin}} = R_d/f(q)$. Thus, considering ingresses or egresses for the Roche-lobe-filling case, we have $\mathcal{F}_{\text{in-eg}} = f(q)$. Typical values of $f(q)$ are on the order of a few tenths. Thus, because the Roche-lobe-filling donor's size is just a few times smaller than the orbital separation, the probability that the orbital orientation is favourable for eclipse is high.

The high rate of mass transfer in ultraluminous XRSs means that either the donor is filling its Roche lobe or it is emitting copious winds that are focused towards the accretor, implying that the donor is nearly filling its Roche lobe. We therefore introduce another factor,

$$\alpha = f(q) \frac{R_d}{R_L}. \quad (14)$$

For Roche-lobe filling, $\alpha = f(q)$, but if the donor is not filling its Roche lobe the value of α can be slightly smaller. With this definition, a convenient way to express $\mathcal{F}_{\text{in-eg}}$ is

$$\mathcal{F}_{\text{in-eg}} = 0.2 \left[\frac{\alpha}{0.2} \right]. \quad (15)$$

The probability of detecting an eclipse ingress or an eclipse egress is therefore given by the general expression below, where the factors are given in equations (15) and (12).

$$\mathbb{P}_{\text{in-eg}} = \mathcal{F}_{\text{in-eg}} \times \mathcal{P}_{\text{in-eg}}. \quad (16)$$

If, therefore, we monitor the light curves of binaries with properties similar to those of M51-ULS-1, there is a probability that can be as high as a few tenths that we will detect an ingress, and the same probability for an egress. This relatively high probability supports the hypothesis that the candidates for ingress and egress we considered in Extended Data Fig. 6 are what they appear to be, and that we are therefore viewing M51-ULS-1 along its orbital plane to within an angle R_d/a_{bin} . Note that this relatively high probability is borne out by observations, in that there are at least two additional eclipsing XRBs in the Chandra field containing M51-ULS-1 (ref. ²⁷).

Transits. The circumbinary planet candidate has a wider orbit and consequently a longer orbital period than the binary.

$$P_{\text{orb}} = 68 \text{ yr} \left[\frac{a_{\text{orb}}}{45 \text{ au}} \right]^{\frac{3}{2}} \left[\frac{20 M_{\odot}}{M_{\text{tot}}} \right]^{\frac{1}{2}}. \quad (17)$$

This makes the temporal factor for the detection of a transit smaller.

$$\mathcal{P}_{\text{trans}} = 4.7 \times 10^{-4} \left[\frac{T_{\text{obs}}}{1 \text{ Ms}} \right] \left[\frac{45 \text{ au}}{a_{\text{pl}}} \right]^{\frac{3}{2}} \left[\frac{M_{\text{tot}}}{20 M_{\odot}} \right]^{\frac{1}{2}}. \quad (18)$$

If the orientation of the orbital plane relative to our line of sight is arbitrary, then direct computation of the spatial factor gives

$$\mathcal{F}_{\text{trans}} = 1.2 \times 10^{-5} \left[\frac{(R_X + R_{\text{ec}})}{2 R_J} \right] \left[\frac{45 \text{ au}}{a_{\text{pl}}} \right]. \quad (19)$$

In this case, $\mathcal{P}_{\text{trans}} \times \mathcal{F}_{\text{trans}}$ is on the order of one part per billion, indicating that there could be a billion planets for each discovered.

Note that the calculation above can be viewed only as a rough example. To compute the true probabilities we must integrate over the distributions of the physical parameters. These distributions are presently unknown. When, however, multiple planets orbiting XRBs have been found, we will begin to develop physically reasonable distributions. This is analogous to the situation after the first discovery of gravitational mergers³³.

If, however, the binary is eclipsing, we know that the binary orbital plane is roughly aligned with our line of sight. One may hypothesize that any planets orbiting an XRB are likely to have orbital planes roughly aligned with the binary's orbital plane. Alignment is generally expected for the circumbinary disks in which planets form, and this is consistent with observations of circumbinary planets³⁴. A recent example of a coaligned system of circumbinary planets is Kepler-47 (ref. ³⁵). We don't know if the same should be true for planets orbiting XRBs. If the

planetary and binary orbits were initially aligned, a later event such as a supernova could disrupt the alignment. It is also possible for alignment to be enhanced or restored by mass loss from the binary. Mass loss directed along the binary plane can, for example, drive a planet towards the midplane. We note, though, that important elements of the processes involved in binary evolution are not yet well understood, and discussions of possible alignment therefore remain speculative.

Should even rough alignment be common, transits are more likely to be detected in eclipsing XRBs. This hypothesis will be tested through observations that tell us whether planetary or other substellar transits are detected only or primarily in eclipsing binaries. Here, we consider what such a finding would mean for the computation of probabilities from observations. As we saw above, if the orientation of the orbital plane with respect to our line of sight is random, $\mathcal{F}_{\text{trans}}$ is very small. If, however, coplanarity of planetary and stellar orbits were strictly enforced by nature, then, given a planet orbiting an XRB observed to be eclipsing, our probability of detecting the planet's transit would simply be given by $\mathcal{P}_{\text{trans}}$. We can take this latter possibility into account without sacrificing the possibility of random orientations by expressing the probability of detecting a transit as follows:

$$\mathbb{P}_{\text{trans}} = g \times \mathcal{F}_{\text{in-eg}} \times \mathcal{P}_{\text{trans}}. \quad (20)$$

The value of the factor g is unity if exact coplanarity holds. If planetary and binary orbital orientations are random, $g = \mathcal{F}_{\text{trans}}/\mathcal{F}_{\text{in-eg}}$. Note that even if coplanarity is common, it is unlikely to be exact, and note that observing both eclipses and transits in a single system is consistent with values of g smaller than unity.

There are enough X-ray data presently available to suggest that additional planets can be discovered through archival searches (see 'Galactic populations of planets and prospects for future observations'). Meanwhile, new data are being collected, and future missions such as Lynx and Athena will substantially increase the data rate. Consider that $N_{\text{pl,obs}}$ have been discovered. We will be able to estimate the number of planets per XRB, $\frac{N_{\text{pl}}}{N_{\text{XRB}}}$, in the surveyed XRB populations by using the probability relationships. Below, $N_{\text{XRB,obs}}$ is the number of bright XRBs observed for roughly comparable exposure times in our archival survey. For the work in this paper, roughly 200 bright XRB had exposure times close to 1 Ms. The number of planets per XRB is

$$\frac{N_{\text{pl}}}{N_{\text{XRB}}} = \frac{N_{\text{pl,obs}}}{g \times \mathbb{P}_{\text{trans}} \times N_{\text{XRB,obs}}}. \quad (21)$$

With the observation of only one object, the uncertainty limits on $N_{\text{pl,obs}}$ are large, and the characteristics of the distributions over which we should integrate to derive $\mathbb{P}_{\text{trans}}$ are unknown. This makes a realistic determination of the average number of planets per XRB impossible. We can draw one conclusion based on the discovery of exoplanet M51-1 (M51-ULS-1), namely that planets around XRBs must be fairly common. If we use the albeit highly uncertain value of $\mathbb{P}_{\text{trans}} = 5 \times 10^{-4}$, then for 200 observed XRBs we obtain the estimate $\frac{N_{\text{pl}}}{N_{\text{XRB}}} \approx \frac{10}{g}$. Future searches for transits will either place limits on this quantity or measure its value.

Physically realistic estimates of g will require the discovery of additional transiting planets or brown dwarfs. Note in addition that the ratio of the numbers of wide-orbit planets and brown dwarfs will be determined by the distributions of measured transit properties.

Data availability

The Chandra and XMM-Newton data that support the findings of this study are available from the Chandra Data Archive site <https://cda.harvard.edu/chaser/> and the HEASARC website <https://heasarc.gsfc.nasa.gov/docs/archive.html>, respectively. The ObsIDs of the 24 observations employed in this work are listed in Extended Data Fig. 1, which images a table of the X-ray observations.

Code availability

We have made available all scripts and extracted data used to run the MCMC and hardness ratio analyses in a Google Drive folder at https://drive.google.com/drive/folders/1c1O8q8wokWPbyNxRnkpXYS70eBFmL_80?usp=sharing hosted by the Center for Astrophysics | Harvard & Smithsonian. The scripts use several routines in PINTofALE <https://hea-www.harvard.edu/PINTofALE/>. The hardness ratio code BEHR, used in the 'Nature of the X-ray dip' section, is available at <https://hea-www.harvard.edu/AstroStat/BEHR/>.

Received: 10 September 2020; Accepted: 18 August 2021;

Published online: 25 October 2021

References

1. Iimura, N. & Di Stefano, R. Searching for exoplanets around X-ray binaries with accreting white dwarfs, neutron stars, and black holes. *Astrophys. J.* **859**, 40 (2018).
2. Jaodand, A., Hessels, J. W. T. & Archibald, A. A decade of transitional millisecond pulsars. In *Proc. International Astronomical Union Symposium 337* Vol. 13 (eds Weltevrede, P. et al.) 47–51 (Cambridge Univ. Press, 2018)..

3. Wolszczan, A. Discovery of pulsar planets. *New Astron. Rev.* **56**, 2–8 (2012).
4. Lorimer, D. Binary and millisecond pulsars. *Living Rev. Relativ.* **11**, 8 (2008).
5. Ford, E. B., Joshi, K. J., Rasio, F. A. & Zabarsky, B. Theoretical implications of the PSR B1620-26 triple system and its planet. *Astrophys. J.* **528**, 336–350 (2000).
6. Di Stefano, R. & Kong, A. K. H. Luminous supersoft X-ray sources in external galaxies. *Astrophys. J.* **592**, 884–899 (2003).
7. Urquhart, R. & Soria, R. Optically thick outflows in ultraluminous supersoft sources. *Mon. Not. R. Astron. Soc.* **456**, 1859–1880 (2016).
8. Terashima, Y., Inoue, H. & Wilson, A. S. Hubble Space Telescope identification of the optical counterparts of ultraluminous X-ray sources in M51. *Astrophys. J.* **645**, 264–270 (2006).
9. Rappaport, S. A., Podsiadlowski, P. & Pfahl, E. Stellar-mass black hole binaries as ultraluminous X-ray sources. *Mon. Not. R. Astron. Soc.* **356**, 401–414 (2005).
10. Parmar, A. N., White, N. E., Giommi, P. & Gottwald, M. The discovery of 3.8 hour periodic intensity dips and eclipses from the transient low-mass X-ray binary EXO 0748-676. *Astrophys. J.* **308**, 199–212 (1986).
11. Gambino, A. et al. Updating the orbital ephemeris of the dipping source XB 1254-690 and the distance to the source. *Res. Astron. Astrophys.* **17**, 108 (2017).
12. Church, M. J. et al. Progressive covering in dipping and Comptonization in the spectrum of XB 1916-053 from the BeppoSAX observation. *Astron. Astrophys.* **338**, 556–562 (1998).
13. Humphrey, P. J., Church, M. J., Baucińska-Church, M. & Parmar, A. N. Spectral evolution during dipping in X 1624-490 from the BeppoSAX observation. *AIP Conf. Proc.* **599**, 658–661 (2001).
14. Park, T. et al. Bayesian estimation of hardness ratios: modeling and computations. *Astrophys. J.* **652**, 610–628 (2006).
15. Greiner, J. & Di Stefano, R. X-ray off states and optical variability in CAL 83. *Astron. Astrophys.* **387**, 944–954 (2002).
16. Bayliss, D. et al. NGTS-1b: a hot Jupiter transiting an M-dwarf. *Mon. Not. R. Astron. Soc.* **475**, 4467–4475 (2018).
17. Barfée, I., Chabrier, G., Barman, T. S., Allard, F. & Hauschildt, P. H. Evolutionary models for cool brown dwarfs and extrasolar giant planets. The case of HD 209458. *Astron. Astrophys.* **402**, 701–712 (2003).
18. Stevens, D. J. et al. An extreme-mass ratio, short-period eclipsing binary consisting of a B dwarf primary and a pre-main-sequence M star companion discovered by KELT. *Mon. Not. R. Astron. Soc.* **499**, 3775–3791 (2020).
19. Triaud, A. H. M. J. et al. The EBLM Project. IV. Spectroscopic orbits of over 100 eclipsing M dwarfs masquerading as transiting hot Jupiters. *Astron. Astrophys.* **608**, A129 (2017).
20. Carmichael, T. W., Latham, D. W. & Vanderburg, A. M. New substellar discoveries from Kepler and K2: is there a brown dwarf desert? *Astron. J.* **158**, 38 (2019).
21. Owen, J. E. & Campos Estrada, B. Testing exoplanet evaporation with multitransiting systems. *Mon. Not. R. Astron. Soc.* **491**, 5287–5297 (2020).
22. Poppenhaeger, K., Ketzer, L. & Mallonn, M. X-ray irradiation and evaporation of the four young planets around V1298 Tau. *Mon. Not. R. Astron. Soc.* **500**, 4560–4572 (2021).
23. Sanz-Forcada, J., Desidera, S. & Micela, G. Effects of X-ray and extreme UV radiation on circumbinary planets. *Astron. Astrophys.* **570**, A50 (2014).
24. Fruscione, A. et al. CIAO: Chandra's data analysis system. In *Proc. Society of Photo-Optical Instrumentation Engineers (SPIE) Conference on Astronomical Telescopes and Instrumentation* Vol. 6270 (eds Silva, D. R. & Doxsey, R. E.) (SPIE, 2006).
25. Blackburn, J. K. FTOOLS: a FITS data processing and analysis software package. *ASP Conf. Ser.* **77**, 367–370 (1995).
26. Wang, S., Soria, R., Urquhart, R. & Liu, J. Discovery of two eclipsing X-ray binaries in M 51. *Mon. Not. R. Astron. Soc.* **477**, 3623–3645 (2018).
27. Urquhart, R. & Soria, R. Two eclipsing ultraluminous X-Ray sources in M51. *Astrophys. J.* **831**, 56 (2016).
28. Irwin, J. et al. Ultraluminous X-ray bursts in two ultracompact companions to nearby elliptical galaxies. *Nature* **538**, 356–358 (2016).
29. Gelman, A. et al. *Bayesian Data Analysis* 3rd edn (CRC Press, 2013).
30. Kaastra, J. S. On the use of C-stat in testing models for X-ray spectra. *Astron. Astrophys.* **605**, A51 (2017).
31. Einstein, A. Lens-like action of a star by the deviation of light in a gravitational field. *Science* **84**, 506–507 (1936).
32. Eggleton, P. P. Approximations to the radii of Roche lobes. *Astrophys. J.* **268**, 368–369 (1983).
33. Abbott, B. P. et al. Astrophysical implications of the binary black hole merger GW150914. *Astrophys. J. Lett.* **818**, L22 (2016).
34. Foucart, F. & Lai, D. Evolution of linear warps in accretion discs and applications to protoplanetary discs in binaries. *Mon. Not. R. Astron. Soc.* **445**, 1731–1744 (2014).
35. Orosz, J. A. et al. Discovery of a third transiting planet in the Kepler-47 circumbinary system. *Astron. J.* **157**, 174 (2019).

Acknowledgements

R.D. thanks D. D'Orazio and T. Hutchinson-Smith for relevant discussions and input on the analysis of X-ray light curves. She would also like to thank A. Burrows and D. Charkrabarty for discussions about the models, and D. Latham for a discussion about the light curve interpretation. We thank P. Edmonds and M. Watzke for useful discussions. J.B. thanks D. Alp for discussion and help with software in the process of analysing images, and the Center for Excellence in Education's Research Science Institute for enabling collaboration with R.D. T.W.C. thanks D. Latham and his research group for discussions and guidance on transiting brown dwarfs. V.L.K. thanks T. Gaetz and P. Sharda for useful discussions on the maths of overlapping circles. V.L.K. acknowledges support from NASA contract NAS8-03060 to the Chandra X-ray Center. T.W.C. thanks the National Science Foundation Graduate Research Fellowships Program for providing funding for this work. N.I. thanks the John Harvard Distinguished Science Fellows Program for research support.

Author contributions

R.D. initiated and coordinated the work, recruited the team, conducted initial fits to the X-ray light curve and worked on all elements of the modelling and interpretation, as well as on the manuscript. J.B. participated in our initial analysis of the X-ray light curves discovering the short eclipse; she found a journal article (authored by R.U. and R.D.) in which the eclipse light curve was shown but not analysed. She participated in many aspects of the complete analysis as well as in manuscript preparation. R.U. downloaded, processed and analysed all of the X-ray data used in this project. He plotted and studied both the long-term and short-term light curves and provided the information and background needed to interpret the data. R.S. provided input into the relation between the XRS M51-ULS-1, the model for this source, and its connection to other XRSs. He contributed to key elements of the modelling and interpretation. V.L.K., an expert in astrostatistics and X-ray data analysis, made several figures, worked on the text in various places and provided crucial advice on various model elements. T.W.C., an expert in brown-dwarf transits, developed the input and figures on astrophysical objects with sizes similar to those of the candidate exoplanet. He also played a significant role in preparing the manuscript for publication. N.I., an expert in star formation, worked on the binary and planet models and provided necessary input on star formation.

Competing interests

The authors declare no competing interests.

Additional information

Extended data is available for this paper at <https://doi.org/10.1038/s41550-021-01495-w>.

Correspondence and requests for materials should be addressed to Rosanne Di Stefano.

Peer review information *Nature Astronomy* thanks the anonymous reviewers for their contribution to the peer review of this work.

Reprints and permissions information is available at www.nature.com/reprints.

Publisher's note Springer Nature remains neutral with regard to jurisdictional claims in published maps and institutional affiliations.

© The Author(s), under exclusive licence to Springer Nature Limited 2021

ObsID (1)	Observatory (2)	Exp time (ks) (3)	Date (4)	Date in MJD (5)
354	Chandra	14.86	2000-06-20	51715.34 - 51715.51
1622	Chandra	26.81	2001-06-23	52083.78 - 52084.09
112840201	XMM	20.916	2003-01-15	52654.55 - 52654.79
3932	Chandra	47.970	2003-08-07	52858.60 - 52859.16
212480801	XMM	49.214	2005-07-01	53552.28 - 53552.85
303420101	XMM	54.114	2006-05-20	53875.27 - 53875.90
303420201	XMM	36.809	2006-05-24	53879.47 - 53879.89
677980701	XMM	13.319	2011-06-07	55719.21 - 55719.36
677980801	XMM	13.317	2011-06-11	55723.20 - 55723.35
12562	Chandra	9.63	2011-06-12	55724.29 - 55724.40
12668	Chandra	9.99	2011-07-03	55745.44 - 55745.55
13813	Chandra	179.2	2012-09-09	56179.74 - 56181.82
13812	Chandra	157.46	2012-09-12	56182.77 - 56184.59
15496	Chandra	40.97	2012-09-19	56189.39 - 56189.86
13814	Chandra	189.85	2012-09-20	56190.31 - 56192.50
13815	Chandra	67.18	2012-09-23	56193.34 - 56194.12
13816	Chandra	73.1	2012-09-26	56196.22 - 56197.06
15553	Chandra	37.57	2012-10-10	56210.03 - 56210.47
19522	Chandra	37.76	2017-03-17	57829.03 - 57829.47
824450901	XMM	78.0	2018-05-13	58251.89 - 58252.79
830191401	XMM	98.0	2018-05-25	58263.85 - 58264.99
830191501	XMM	63.0	2018-06-13	58282.07 - 58282.80
830191601	XMM	63.0	2018-06-15	58284.06 - 58284.79
20988	Chandra	19.82	2018-08-31	58185.06 - 58553.76

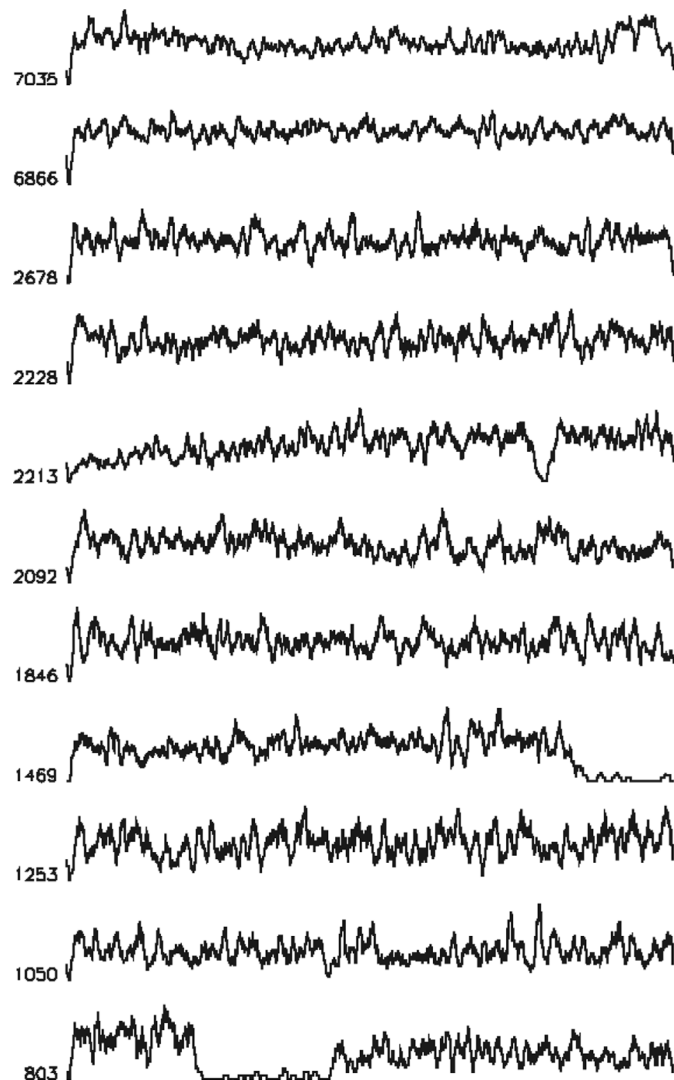
(1) Observation ID; (2) observatory; (3) source exposure time; (4) observation date; (5) start and end of observation in modified Julian days.

Extended Data Fig. 1 | X-Ray Observation.

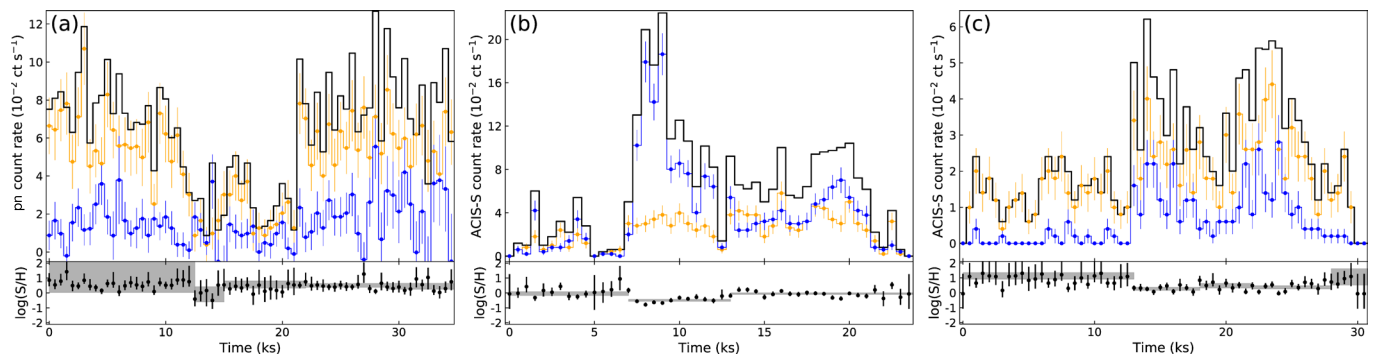
ObsID (1)	Average count rate (10^{-3} ct s $^{-1}$) (2)	In eclipse (ks) (3)	Out of eclipse (ks) (4)
354	6.4 ± 0.4	0	14.86
1622	4.9 ± 0.3	0	26.81
112840201	5.1 ± 0.2	0	20.916
3932	7.2 ± 0.2	0	47.970
212480801	9.5 ± 0.3	0	49.214
303420101	< 0.6	—	—
303420201	6.0 ± 0.2	0	36.809
677980701	2.0 ± 0.3	0	13.319
677980801	< 3.5	0	13.317
12562	< 1.2	—	—
12668	< 1.2	—	—
13813	6.1 ± 0.2	0	179.2
13812	7.8 ± 0.2	0	157.46
15496	7.6 ± 0.5	0	40.97
13814	12.4 ± 0.3	~10.0	~179.85
13815	13.0 ± 0.5	~12.0	~55.18
13816	0.7 ± 0.2	0	73.1
15553	< 0.7	—	—
19522	1.1 ± 0.2	0	37.76
824450901	7.5 ± 0.3	~44.4	~33.6
830191401	< 1.0	0	98.0
830191501	6.0 ± 0.1	0	63.0
830191601	7.8 ± 0.2	0	63.0
20988	5.0 ± 2.0	0	19.82

(1) Observation ID; (2) photon counts during active exposure; (3) time spent in eclipse; (4) time spent out of eclipse. Dashes indicate low count rates or possible “off” state.

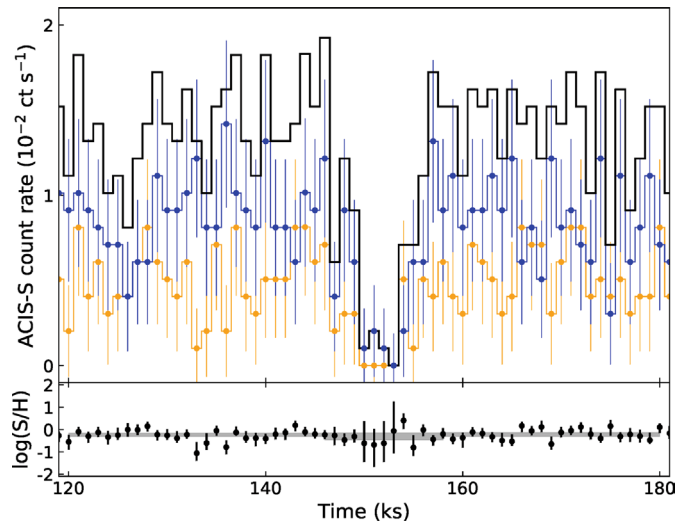
Extended Data Fig. 2 | X-Ray Count Rates.



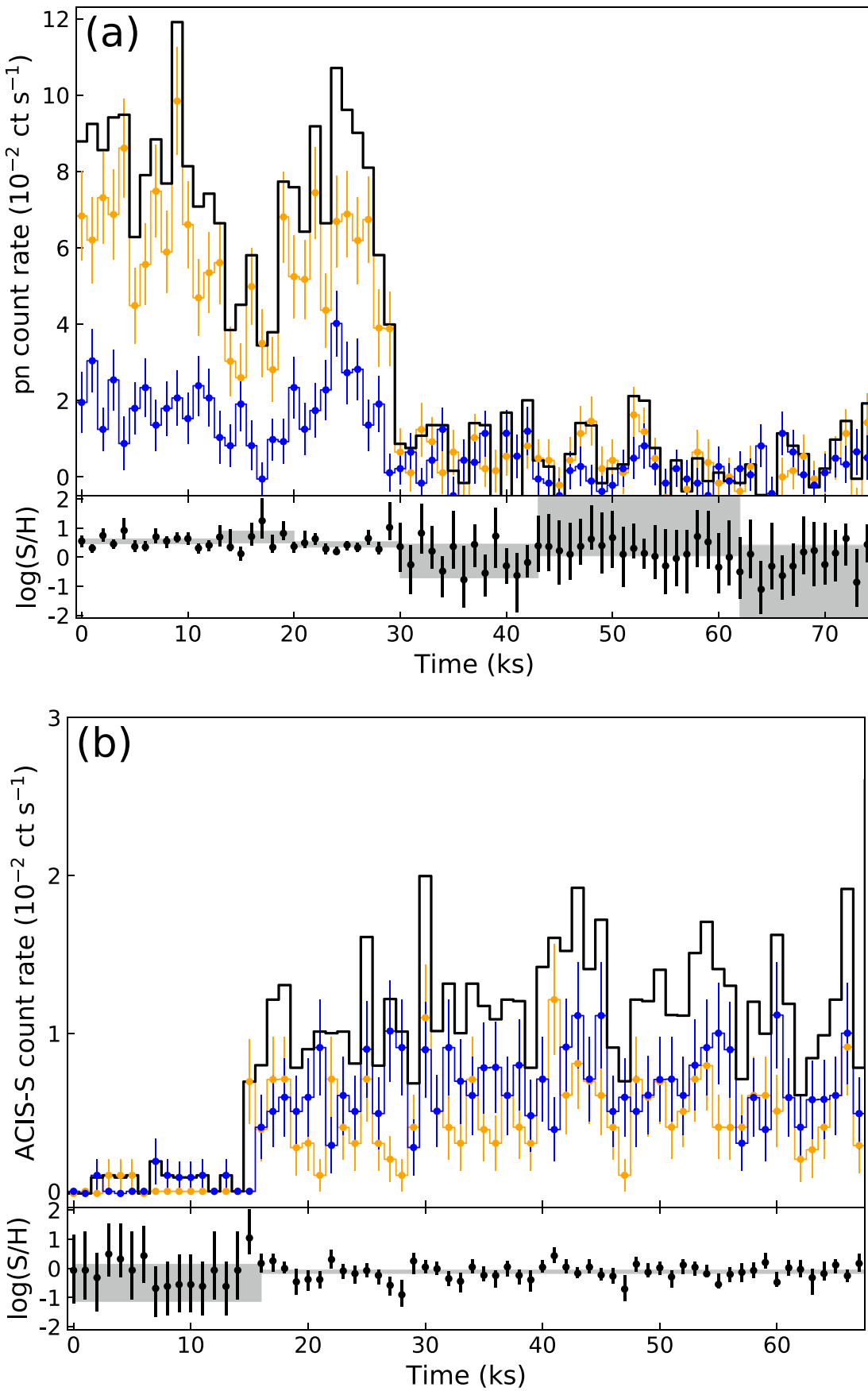
Extended Data Fig. 3 | Sparklines. Sparklines of light curves from variable sources in M51 with >800 counts found in Chandra ObsID 13814. The x-axis covers the same time range as in the bottom panel of Figure 1. The total counts in each light curve is shown at left. The source we focus on here, M51-ULS-1, is the fifth from the top, with 2213 counts. Other sources of note include the ingress of an eclipsing ULX(ULX-1 from²⁷, fourth from bottom, with 1489 counts), and an eclipsing neutron star XRB(S2 from²⁶, at bottom, with 803 counts).



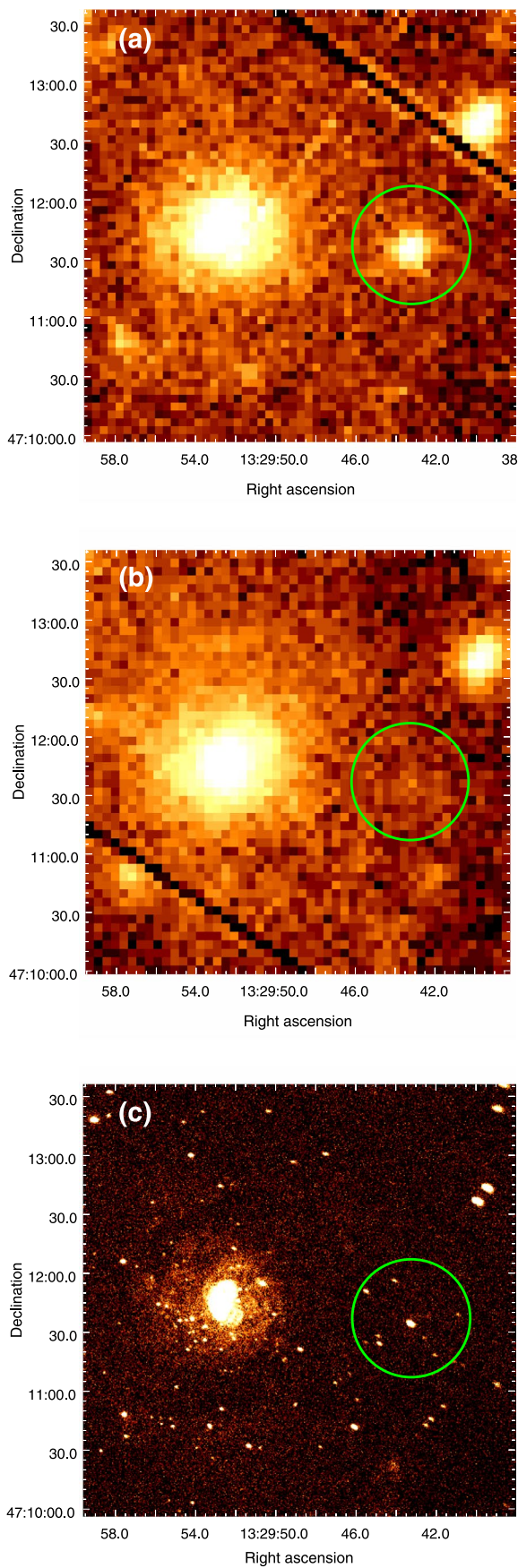
Extended Data Fig. 4 | Accretion Dips. Exemplar X-ray observations of accretion-related dips, showing the background subtracted light curves in several bands in the upper part of each panel, and the spectral colour in the lower part. The sources shown are: Panel (a); a double-dip found in M51-ULS-1 (XMM-Newton observation 303420201); Panel (b): M101-ULS (*Chandra* ObsID 4737); Panel (c): M101-ULS (*Chandra* ObsID 5338). The black light curves are for the broad band (0.2–10 keV), comprised of the soft ($S=0.2:0.7$ keV; orange histograms) and hard ($H=0.7:10$ keV; blue histograms) passbands. The corresponding spectral colour $C = \log \frac{S}{H}$ is shown in the lower part of each panel, with 90% highest-posterior density (HPD) error bars estimated using Park et al.¹⁴. The average colour over some intervals of interest corresponding to light curve behavior are shown as the shaded regions. Unlike the short-duration event seen in M51-ULS-1 (see Figure 4), the intensity variations are stochastic and the spectrum displays variations correlated with intensity.



Extended Data Fig. 5 | The Transit. The putative eclipse event studied here, shown in analogy to Extended Data Figure 4 above. The sizes of the error bars increase for low count rates, but there is no evidence for spectral variations across the transit.

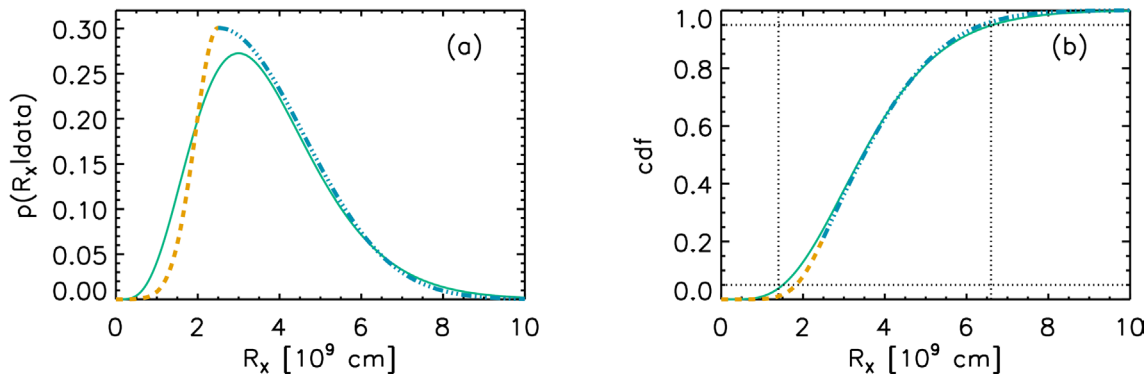


Extended Data Fig. 6 | Ingress to and Egress from Eclipse of M51-ULS-1 by the Donor Star. Light curves of occultation events by the companion star. Panel (a): As in Extended Data Fig. 4, but for intervals in M51-ULS-1 that appear to show long-duration eclipse ingress during the *XMM-Newton* observation 824450901. Panel (b): as above, but for an eclipse egress during *Chandra* ObsID 13815.

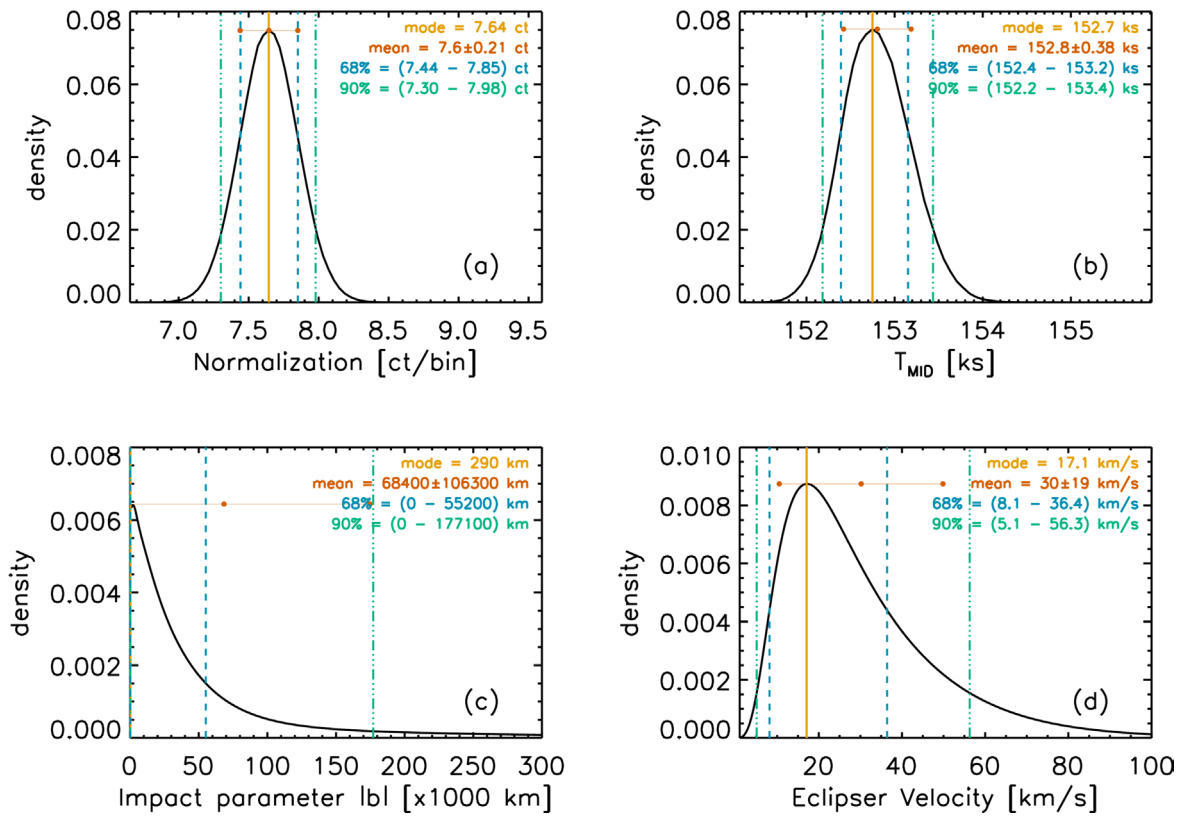


Extended Data Fig. 7 | See next page for caption.

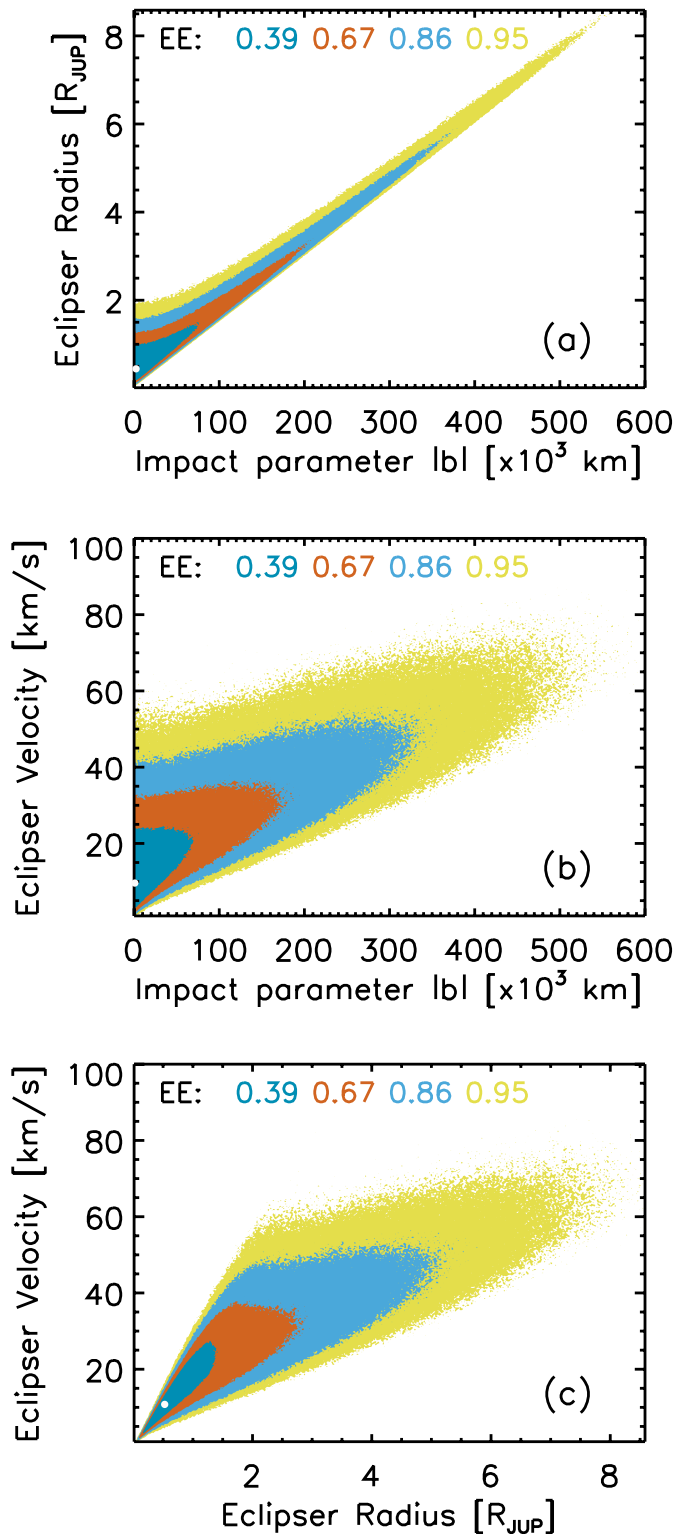
Extended Data Fig. 7 | X-Ray Images of the Field containing M51-ULS-1. XMM-Newton image of M51-ULS-1 during eclipse. Panel (a): XMM-Newton/pn 0.2–10 keV image of the observation 303420201 during which M51-ULS-1 appears active. Panel (b): as in the upper panel, but for the portion of XMM-Newton observation 824450901 in which the source is in eclipse (i.e., ~30–75 ks in Extended Data Fig. 6, top). Panel (c): stacked 0.3–7 keV *Chandra*/ACIS image of the same field. The 25'' radius green circles in each image is comparable to the XMM-Newton extraction region for M51-ULS-1. It is clear from the *Chandra* image that a number of nearby point sources are likely contaminating the XMM-Newton extraction region for M51-ULS-1 and may be causing the residual hard emission seen while the source is in eclipse.



Extended Data Fig. 8 | Probability Distributions of the Radius of the Source. The nominal probability distribution of R_x . Panel **(a)** shows the differential density distributions for the conjoined half-Gaussians (orange dashed curve on left and blue dash-triple-dotted curve on right) and for a gamma distribution (green solid line). Panel **(b)** shows the cumulative distributions of the two candidate distributions (as in Panel **(a)**), along with vertical dotted lines indicating the 5% and 95% bounds of R_x , and horizontal dashed lines indicating the corresponding levels. The gamma distribution matches the bounds better, but has a slightly larger mode.



Extended Data Fig. 9 | Marginalized Posterior Probability Density Distributions of Eclipse Model Parameters. The marginalized posterior probability density distributions of eclipse model parameters **(a)** baseline count rate c_x , **(b)** eclipse mid-point T_{mid} , **(c)** impact parameter b , and **(d)** the velocity of the eclipsor. The probability density distributions are shown as thick black curves, with the vertical lines marking the mode (solid orange), 68% highest-posterior-density (HPD) bounds (dashed blue), 90% HPD bounds (dash-triple-dotted green). The values of each of these quantities, along with the mean and 1σ standard deviation (marked as the thin red horizontal bar), are printed in the legend within each panel (see also Table 1). Note that the posterior density distribution of the radius of the eclipsor, R_{ecr} , is shown in Figure 5.



Extended Data Fig. 10 | Joint Posterior Distributions of Pairs of Eclipse Model Parameters. The joint posterior distributions between the parameters for the eclipsor's impact parameter b , radius f_{ecr} and velocity v_{pl} for (a) $p(b, f_{\text{ecr}})$, (b) $p(b, v_{\text{pl}})$, and (c) $p(f_{\text{ecr}}, v_{\text{pl}})$ from top to bottom. Each contour plot shows the joint density, marked at enclosed estimated probability (EE) regions for 39% (bluish green; 2D Gaussian 1σ equivalent), 67% (red; 1.5σ), 85% (sky blue; 2σ), and 95% (yellow; 2.5σ). The solid white dots indicate the mode of the distribution. Note that strong correlations are present between these parameters; see text for discussion.